Very high gas fractions and extended gas reservoirs in z=1.5 disk galaxies

Emanuele Daddi, F. Bournaud, F. Walter, H. Dannerbauer, C. Carilli, M. Dickinson, D. Elbaz, G. E. Morrison, D. Riechers, M. Onodera, et al.

The Astrophysical Journal, 713:686–707, 2010 April 10 doi:10.1088/0004-637X/713/1/686

VERY HIGH GAS FRACTIONS AND EXTENDED GAS RESERVOIRS IN $z = 1.5$ DISK GALAXIES

E. Daddi[1], F. Bournaud[1], F. Walter[2], H. Dannerbauer[1], C. L. Carilli[3], M. Dickinson[4], D. Elbaz[1], G. E. Morrison[5,6], D. Riechers[7], M. Onodera[1], F. Salmi[1], M. Krips[8], and D. Stern[9]

[1] Laboratoire AIM, CEA/DSM-CNRS-Université Paris Diderot, DAPNIA/Service d'Astrophysique, CEA Saclay, Orme des Merisiers, 91191 Gif-sur-Yvette Cedex, France; edaddi@cea.fr
[2] Max-Planck-Institut für Astronomie, Königstuhl 17, D-69117 Heidelberg, Germany
[3] National Radio Astronomy Observatory, P.O. Box 0, Socorro, NM 87801, USA
[4] National Optical Astronomy Observatory, 950 N. Cherry Ave., Tucson, AZ 85719, USA
[5] Institute for Astronomy, University of Hawaii, Honolulu, HI 96822, USA
[6] Canada–France–Hawaii Telescope, Kamuela, HI 96743, USA
[7] Caltech, Pasadena, CA 91109, USA
[8] Institut de Radio Astronomie Millimétrique (IRAM), St. Martin d'Hères, France
[9] Jet Propulsion Laboratory, California Institute of Technology, Pasadena, CA 91109, USA
Received 2009 November 14; accepted 2010 February 22; published 2010 March 24

ABSTRACT

We present evidence for very high gas fractions and extended molecular gas reservoirs in normal, near-infrared-selected (BzK) galaxies at $z \sim 1.5$. Our results are based on multi-configuration CO[2–1] observations obtained at the IRAM Plateau de Bure Interferometer. All six star-forming galaxies observed were detected at high significance. High spatial resolution observations resolve the CO emission in four of them, implying sizes of the gas reservoirs of order of 6–11 kpc and suggesting the presence of ordered rotation. The galaxies have UV morphologies consistent with clumpy, unstable disks, and UV sizes that are consistent with those measured in CO. The star formation efficiencies are homogeneously low within the sample and similar to those of local spirals—the resulting gas depletion times are ∼0.5 Gyr, much higher than what is seen in high-z submillimeter galaxies and quasars. The CO luminosities can be predicted to within 0.15 dex from the observed star formation rates (SFRs) and stellar masses, implying a tight correlation of the gas mass with these quantities. We use new dynamical models of clumpy disk galaxies to derive dynamical masses for our sample. These models are able to reproduce the peculiar spectral line shapes of the CO emission. After accounting for the stellar and dark matter masses, we derive molecular gas reservoirs with masses of $(0.4–1.2)\times10^{11}\ M_{\odot}$. The implied conversion (CO luminosity-to-gas mass) factor is very high: $\alpha_{\rm CO} = 3.6 \pm 0.8$, consistent with a Galactic conversion factor but 4 times higher than that of local ultra-luminous IR galaxies that is typically used for high-redshift objects. The gas mass in these galaxies is comparable to or larger than the stellar mass, and the gas accounts for an impressive 50%–65% of the baryons within the galaxies' half-light radii. We are thus witnessing truly gas-dominated galaxies at $z \sim 1.5$, a finding that explains the high specific SFRs observed for $z > 1$ galaxies. The BzK galaxies can be viewed as scaled-up versions of local disk galaxies, with low-efficiency star formation taking place inside extended, low-excitation gas disks. These galaxies are markedly different than local ULIRGs and high-z submillimeter galaxies and quasars, where higher excitation and more compact gas is found.

Key words: cosmology: observations – galaxies: evolution – galaxies: formation – galaxies: starburst – infrared: galaxies

Online-only material: color figures

1. INTRODUCTION

Over the last decade, deep and wide multiwavelength galaxy surveys have been key in addressing critical issues regarding galaxy evolution. By using a variety of color selection techniques, and deriving photometric and/or spectroscopic redshifts, different galaxy populations have now been probed to unprecedented detail up to at least $z \sim 3$. Also, the history of cosmic star formation as well as the corresponding build-up of stellar mass has now been constrained using different observational approaches.

Less well understood are the physical processes that regulate the star formation activity in these young systems and the question of if and how galaxy star formation at high redshift differs from what is seen in the local universe. While it has been established that star formation rates (SFRs) in galaxies were on average higher in the past and that the cosmic SFR density peaked at $z > 1$ (see, e.g., Le Borgne et al. 2009), it is still a matter of debate how much of this increase is due to more frequent merging/interactions between galaxies, or other processes. Analysis of the ultraviolet (UV) and optical rest-frame morphology and Hα velocity fields of high-redshift galaxies suggest that the galaxies responsible for the bulk of the SFR density at $z \sim 1$–3 are disks (e.g., Bell et al. 2005; Elbaz et al. 2007; Genzel et al. 2008). These findings confirmed early hints for the presence of extended disks at high redshift, based on damped Lyα studies (e.g., Wolfe et al. 1986). Some authors, however, advocate a predominant role of mergers based on, e.g., irregularities in high signal-to-noise ratio (S/N) three-dimensional observations of emission lines (e.g., Flores et al. 2006). On the other hand, it is also found that distant star-forming galaxies show irregular morphologies with high clumpiness, especially in the rest-frame UV (e.g., Cowie et al. 1996; Chapman et al. 2003; Daddi et al. 2004b; Elmegreen & Elmegreen 2005). In this context, it is interesting to note that the existence of such bright clumps can explain the observed

kinematic irregularities in high-z galaxies (i.e., without the need to require the presence of mergers; Immeli et al. 2004; Bournaud et al. 2008). More direct evidence for an important role of in situ, quiescent star formation in distant galaxies came from the estimate that the duty cycle of star formation is high in massive $z \sim 2$ galaxies (Daddi et al. 2005, 2007a; see also Caputi et al. 2008), with typical durations of ≈0.5–1 Gyr. This is much longer than the typical duration expected for starbursts ($\lesssim$100 Myr) triggered by mergers, based on simulations (e.g., Mihos & Hernquist 1996; Di Matteo et al. 2008) and also on the observed gas consumption timescales for IR luminous merging galaxies (e.g., Downes & Solomon 1998).

A recent major step forward in characterizing the nature of star formation in distant galaxies was based on the discovery that star-forming galaxies define a narrow locus in the stellar mass–SFR plane (in this paper we will refer to the ratio of SFR to stellar mass as the specific SFR, SSFR). This correlation has been estimated to have a slope of 0.7–1.0 in log space and a dispersion of a factor of only ∼2 from redshifts $z \sim 0.1$ to $z \sim 3.0$ (Noeske et al. 2007; Elbaz et al. 2007; Daddi et al. 2007a; Magdis et al. 2010).

The normalization in this correlation, i.e., the SSFR at a given stellar mass, is higher by a factor of 30 at $z = 2$–3 compared to the local universe. At even higher redshifts, the situation is unclear as the SFRs are typically less well constrained (as they are primarily based on UV luminosities). However, the available data are still consistent with the picture that the correlation extends to earlier epochs ($3.5 < z < 7$) with a normalization similar to that seen at $z = 2$ (Daddi et al. 2009b; Stark et al. 2009; Gonzalez et al. 2009). The existence of this correlation has major implications for our understanding of galaxy formation. For example, the cosmic evolution of the normalization of the relation (Daddi et al. 2009b; Pannella et al. 2009; Gonzalez et al. 2009) is similar to the cosmic evolution of the SFRD (Hopkins & Beacom 2006, 2008; Le Borgne et al. 2009, etc.). It is possible in fact to describe most of the SFRD evolution as the combined result of the evolution of the stellar mass–SFR correlation and that of the space densities (e.g., the mass/luminosity functions) of galaxies. The possible peak at $z \sim 2.5$–3 (Pannella et al. 2009; Magdis et al. 2010; Daddi et al. 2009b) of the SSFRs is thus likely more fundamentally related to the physics underlying galaxy formation than the peak at $z > 1$ of the SFRD evolution, as it is hinting at a change in the physical processes that regulate star formation.

The remarkable tightness of this relation implies a very high degree of homogeneity in these galaxies. In other words, despite the physical complexity of the process by which stars are formed, for a normal, near-IR-selected star-forming galaxy, the SFR is ultimately linked to its stellar mass (which in itself is presumably related to the mass of the underlying dark matter halo).

In order to make further progress in understanding how galaxy formation proceeds in distant galaxies, and to shed light on the origin of the stellar mass–SFR correlations, we need to start probing the properties of molecular gas reservoirs in these galaxies, since it is the molecular gas out of which stars form. If the assembly of galaxies is mostly driven by mergers, one would expect most star formation in merger-driven starbursts with concentrated gas cores (like in submillimeter galaxies) and very efficient star formation, and much less molecular gas and star formation in regular objects. If, on the other hand, most star formation is due to smooth gas flows, then star formation would predominantly take place in more quiescent disk galaxies, accreting gas from their surrounding medium. In addition, one could speculate that the tightness in the stellar mass–SFR correlation might be pointing to homogeneous properties of the molecular gas reservoirs and star formation modes inside the galaxy populations. The increase in the normalization of this correlation with cosmic look-back time could then possibly be simply linked to an increase of the average gas fractions in galaxies, as well as in the ratio of the molecular (H_2) over the atomic (H I) hydrogen fraction (see, e.g., Obreschkow & Rawlings 2009). The presence of massive gas reservoirs seem to be a major requirement for justifying high SFRs, with the lack thereof possibly supporting instead the need for changes in the initial stellar mass function (IMF).

Recently, we reported the detection of large molecular gas reservoirs in two near-IR-selected massive galaxies at $z \sim 1.5$ (Daddi et al. 2008). Based on the knowledge available at the time, i.e., the previously known empirical correlation between CO line luminosity ($L'_{\rm CO}$) and total IR luminosity ($L_{\rm IR}$) those galaxies should not have been detected in CO. However, observations were still attempted based on the results of Daddi et al. (2005, 2007) that suggested a high duty cycle and long duration for star formation in massive high-z galaxies. The subsequent detections of CO[2–1] emission indeed implied low star formation efficiencies (SFEs; defined as the ratio $L_{\rm IR}/L'_{\rm CO}$). These SFEs are similar to what is seen in local spirals and much lower than previously seen in high-redshift galaxies. Subsequent studies revealed low-excitation CO [3–2] to [2–1] line ratios in these galaxies (Dannerbauer et al. 2009) that are more typical of local spirals.

Given that both galaxies were detected in CO, this early result suggested commonplace large molecular gas reservoirs in distant massive galaxies (Daddi et al. 2008). However, improved statistics would clearly be needed in order to formally confirm the result and to estimate the variations in gas properties among the high-z galaxy populations. Higher spatial resolution observations are further required to constrain the sizes of the molecular emission; i.e., given the low SFEs one would expect extended reservoirs rather than the compact emission lines seen in submillimeter-selected galaxies (SMGs) for which Tacconi et al. (2006, 2008) find typically half-light radii of order 2 kpc.

In this paper, we report on low-resolution (D-configuration) observations with the IRAM Plateau de Bure Interferometer (PdBI) of CO[2–1] (redshifted to 3 mm) in four additional BzKs (near-IR-selected galaxies at $z \sim 1.5$) thus tripling the number of sources in our sample. In addition, we report on higher resolution ($\sim$ 1″–1.″5; B-configuration) observations of four galaxies. We also discuss the properties of these six galaxies with respect to the "parent" BzK sample. We use the information gathered on these six galaxies in order to independently constrain the molecular gas mass and, conversely, the infamous CO luminosity-to-gas mass conversion factor $\alpha_{\rm CO}$.

The paper is organized as follows. In Section 2, we present the new PdBI observations and their analysis. In Section 3, we discuss the relation of the six galaxies to the parent sample and the derivation of accurate SFRs and stellar masses. The SFEs are characterized in Section 4 and compared to other galaxy populations. We introduce numerical models of clumpy disks in Section 5 and use the models to calibrate dynamical masses for our sample in Section 6. This section also discusses implications for the implied gas masses and the conversion factors. A discussion and summary of our results is presented in Sections 7 and 8. We apply a concordance *WMAP3* cosmology throughout the paper.

Table 1
Observation Summary Table

Source	R.A.[a] J2000	Decl.[a] J2000	Conf.	Obs. Dates	T_{int}[b] (hr)	Frequency (GHz)	Combined Beam[c]	rms (μJy)[d]
BzK-4171	12:36:26.516	62:08:35.35	D	2007 Apr–Aug	8.2	93.525	$2\farcs05 \times 1\farcs55$, P.A. = 64°	41
			B	2008 Jan–Mar	11.2			
BzK-21000	12:37:10.597	62:22:34.60	D	2007 Apr	6.3	91.375	$1\farcs87 \times 1\farcs60$, P.A. = 64°	51
			B	2008 Jan	6.2			
BzK-16000	12:36:30.120	62:14:28.00	D	2008 May	3.3	91.375	$3\farcs83 \times 3\farcs22$, P.A. = 47°	54
			C	2008 Nov	2.8[e]			
			B	2009 Jan	4.4			
			D	2009 May–Jul	6.5[f]			
BzK-17999	12:37:51.819	62:15:20.16	D	2008 May	6.0	95.501	$1\farcs52 \times 1\farcs30$, P.A. = 96°	41
			B	2009 Jan	6.4			
BzK-12591	12:37:41.371	62:12:51.06	D	2008 May	5.4	88.669	$6\farcs37 \times 5\farcs26$, P.A. = 85°	116
BzK-25536	12:37:28.357	62:18:54.91	D	2008 May	6.2	93.754	$6\farcs32 \times 5\farcs10$, P.A. = 90°	72

Notes.
[a] Coordinates are from VLA 1.4 GHz continuum emission (Morrison et al. 2010). The VLA 1.4 GHz map has a resolution of $1\farcs8$, and the typical position accuracy for our sources is $0\farcs20$.
[b] Equivalent six-antennas on source integration time.
[c] Beam resulting after combining all available configuration and imaging with natural weighting. These are the beams sizes displayed in Figure 1.
[d] Noise per beam averaged over the full 1 GHz spectral range.
[e] Data taken with a primary beam attenuation of 24% while observing the source GN10 (Daddi et al. 2009b).
[f] Data taken with a primary beam attenuation of 40% while observing another source.

2. PDBI OBSERVATIONS AND RESULTS

2.1. Target Selection

The six galaxies that were observed in CO were culled from the sample of Daddi et al. (2007a, 2007b) in the Great Observatories Origins Deep Survey North field (GOODS-N). This sample is based on galaxies selected in the K band down to $K < 20.5$ (Vega scale; or $K < 22.37$ AB), from which we selected the population of star-forming galaxies at $1.4 < z < 2.5$ by using the "star-forming" BzK color criterion of Daddi et al. (2004a) and requiring a detection in deep *Spitzer* imaging at 24 μm. From these galaxies, we chose those that had a pre-determined spectroscopic redshift as required for follow-up observations in CO. Currently, 89 BzK galaxies of the Daddi et al. (2007a, 2007b) sample in GOODS-N have a spectroscopic redshift, from various observing campaigns and from the literature. Among the six targeted galaxies, five redshifts were obtained through our GOODS-N campaigns at Keck using DEIMOS (D. Stern et al. 2010, in preparation). The redshift for BzK-12591 was derived by Cowie et al. (2004). This galaxy, having a strong bulge evident from *Hubble Space Telescope* (*HST*) imaging, has a possible detection of [Ne v]λ3426 Å emission line, suggesting the presence of an active galactic nucleus (AGN). This galaxy is not detected in hard X-ray emission in Alexander et al. (2003) but exhibits some soft X-ray emission. In addition to the availability of a spectroscopic redshift, we also required the detection of the galaxy at 1.4 GHz. This is important because the radio continuum allows us to derive an independent estimate of the SFR in the sources.

2.2. Observations and Data Reductions

Table 1 summarizes the PdBI observations of the six massive, near-IR-selected BzK galaxies at redshifts $1.4 < z < 1.6$ in the GOODS-N (D-configuration data for two galaxies were already presented in Daddi et al. 2008). The frequencies during the observations were tuned to the expected redshifted frequency of CO[2–1].

We used the compact D-configuration of the antennas for detection of the sources, providing the highest sensitivity and lowest spatial resolution ($\sim 5\farcs5$ at our typical frequency of 90 GHz). Four of the sources were followed up at higher resolution ($\sim 1\farcs0$–$1\farcs5$) using the more extended B-configuration. Typical integration times were 5–10 hr per configuration. Most of the observations were obtained with six antennas, with the exception of a few tracks in which only five antennas were available. The correlator has eight independent units, each covering 320 MHz (128 channels each with a width of 2.5 MHz) with a single polarization, resulting in a total bandwidth of about 1 GHz with both polarizations.

We reduced the data with the GILDAS software packages CLIC and MAP, similarly to what is described in Daddi et al. (2008, 2009a, 2009b) and Dannerbauer et al. (2009). Bandpass calibration was performed using observations of the standard calibrators J0418+380 and 3C273. Observations of J1044+719 and J1150+497 were used for phase and amplitude calibration. For flux calibration, we used MWC 349 as a primary calibrator and 3C273 when the former was not available. A model was used to account for the frequency dependence and time variability of the emission of MWC 349. Given the typical observed scatter between the observations and the model for MWC 349, and also comparing the results of flux calibration to the implied antennas efficiency variations, we estimate that the flux calibration is accurate to 10% at 90 GHz.

CO[2–1] emission has been successfully detected at the expected frequency for all six galaxies. Figure 1 shows the detection images (natural weighted, cleaned) averaged over the spectral channels where emission was detected. In all cases, the peak flux is detected at S/N > 5. Figure 2 show the same CO[2–1] contours overlaid on the *HST* images of the galaxies from the GOODS Advanced Camera for Surveys

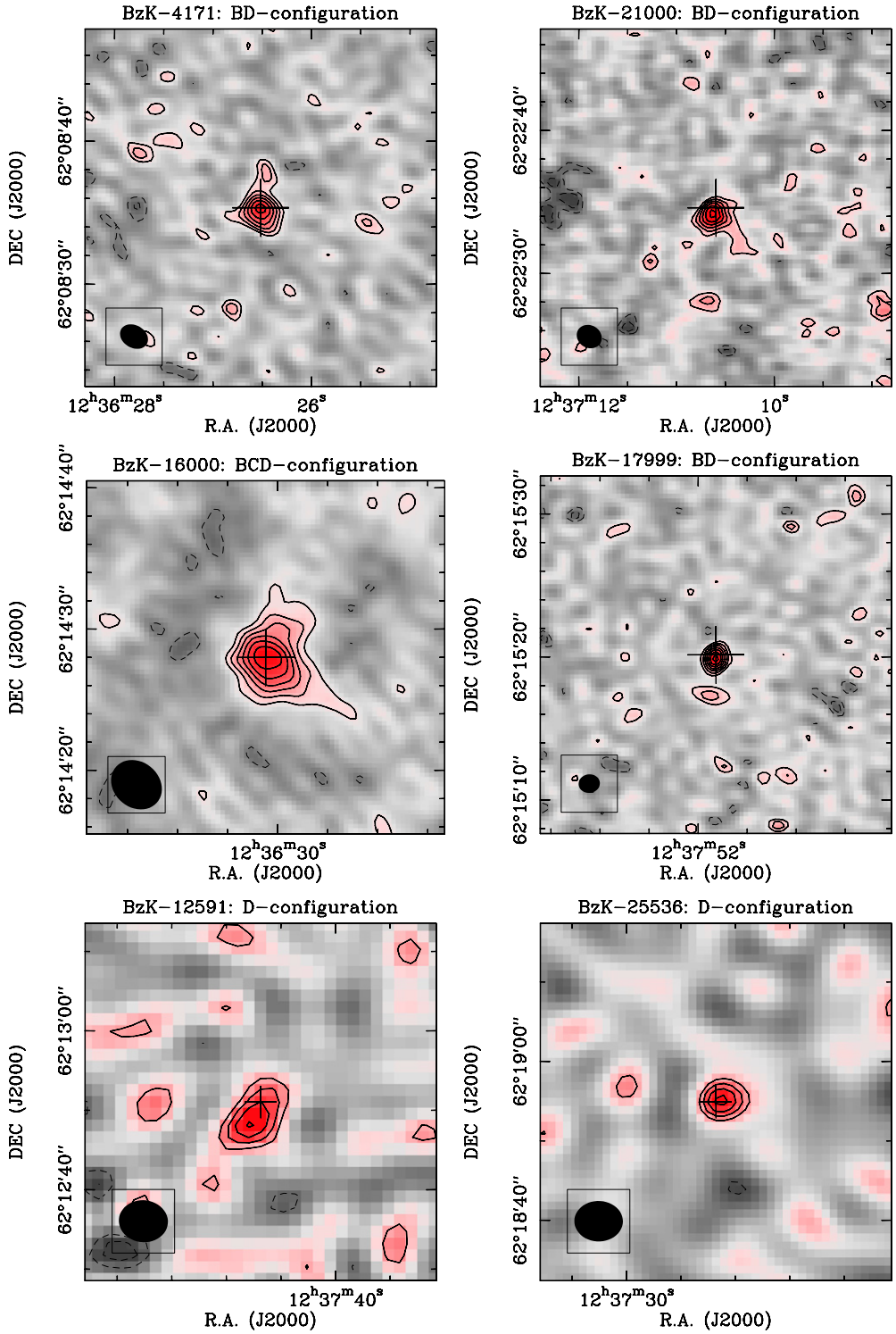

Figure 1. Velocity-averaged maps of the CO[2–1] emission in our sample BzK galaxies. The (cleaned) images were obtained using natural weighting and are based on data from all observations (as indicated on top of the individual panels). Contour levels start at $\pm 2\sigma$ and are in steps of 1σ (see Table 1). The size and orientation of the beam is indicated in the bottom left corner. The panels in the top two rows are 25″ in size, those in the bottom row are 45″ in size. The cross in each panel corresponds to the VLA 1.4 GHz radio continuum position (see Table 1) and is ±2″ (±17 kpc for $z = 1.5$) in size.

(ACS) campaign (Giavalisco et al. 2004). We note that in five of the six cases, the CO[2–1] is very well centered on the VLA 1.4 GHz radio continuum positions (Morrison et al. 2010; crosses in Figure 3) and on the ACS rest-frame ultraviolet images (Figure 2). However, for object BzK-12591 the CO[2–1] detection is offset by about half a beam or $\sim 3''$. The CO[2–1] detection for this galaxy is the one with the lowest S/N and is based only on low-resolution D-configuration data. We conclude that the offset is most likely due to a combination of the effects of noise (we expect uncertainties of 0.″6–1″ at 1σ in the position) and phase instabilities (the interferometric seeing was about 1.″9) during the late-spring observations (Table 1).

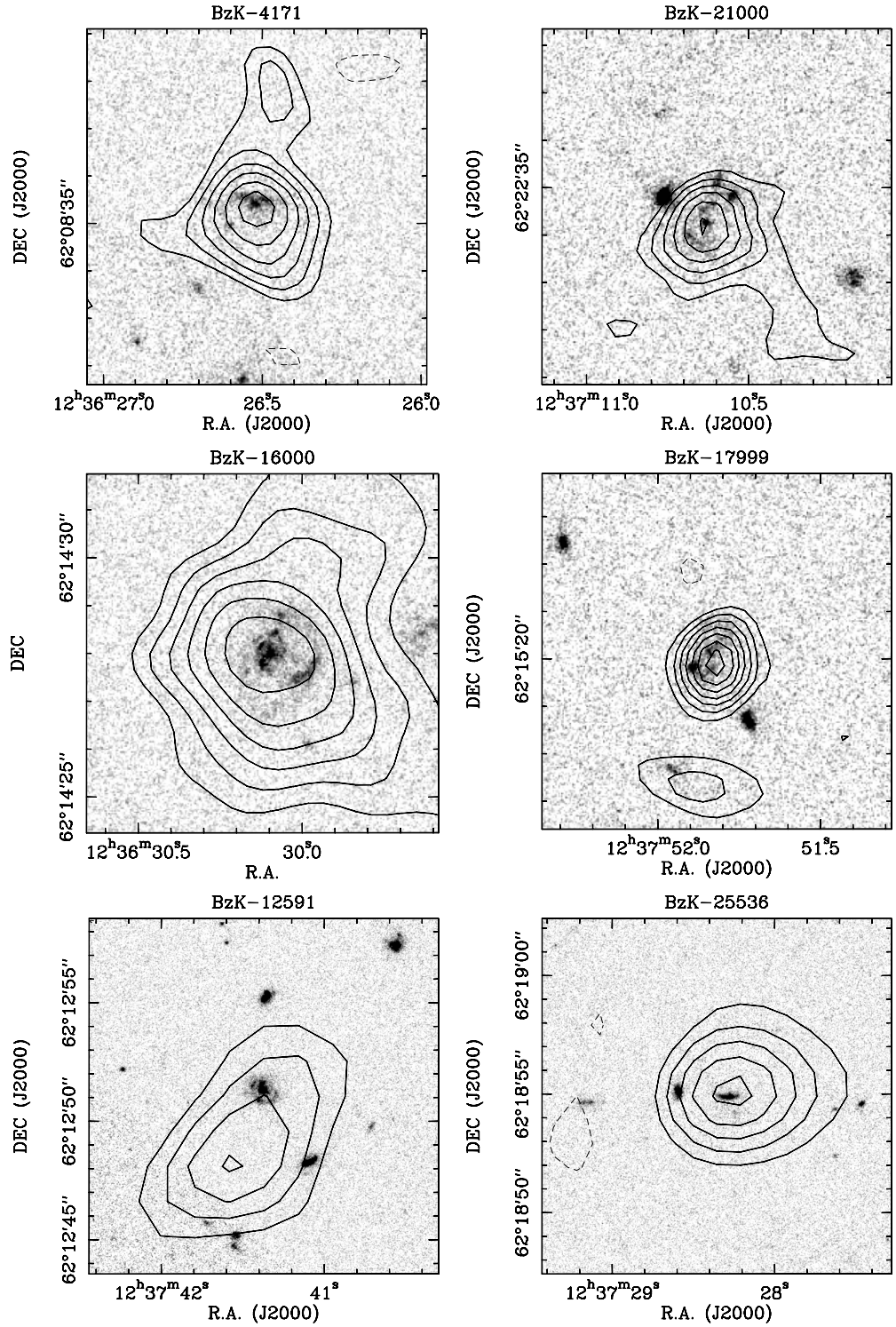

Figure 2. ACS images in the F775W band (*i* band) of the target BzK galaxies. CO[2–1] contours are the same as shown in Figure 1. The panels in the top two rows are 7.″5 in size. The panels in the bottom are 15″ in size. For reference, 1″ subtends 8.5 kpc at $z = 1.5$.

2.3. CO[2–1] Detection Images and Spectra

Figure 3 shows the resulting CO[2–1] spectra binned with a resolution of 25 km s^{-1}. The spectra were obtained by fitting the data in *uv* space with the following procedure: we first averaged the *uv* data over the spectral range in which CO has been detected (see the yellow-shaded regions in Figure 3) to determine the spatial centroid of the CO emission. Keeping this centroid fixed for all channels, we then extracted the spectra with 25 km s^{-1} binning by fitting each channel in the *uv* data. For those objects for which we also have B-configuration data and that appear resolved (BzK-4171, 21000, 16000, and 1799, see next section) we used a circular Gaussian model with a fixed full width at half-maximum (FWHM; derived from the velocity-averaged data). For the remaining two targets (BzK-12591 and 25536), we fitted point source models.

To determine the properties of the CO[2–1] emission (observed flux, velocity centroid, and FWHM), we fitted Gaussian functions to the observed spectra (Figure 3). Several of the

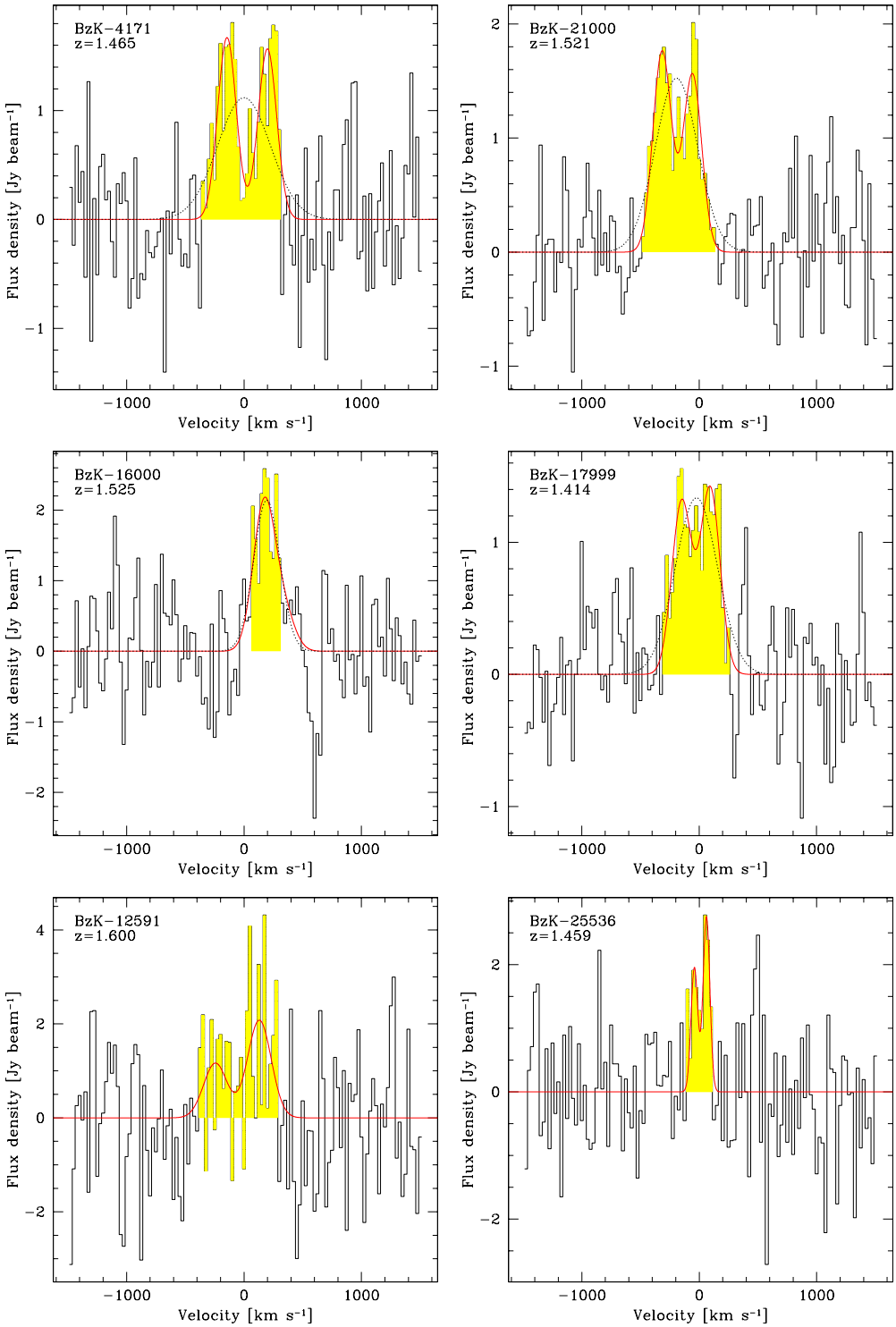

Figure 3. Spectra of CO[2–1] emission binned in steps of 25 km s^{-1}. The yellow color indicates the regions where positive emission is detected. These regions have been used to derive total integrated fluxes and the velocity-averaged maps in Figure 1. The red lines show best-fitting double Gaussian profiles to the spectra (see Table 2 for fit values). In the fits, we forced the FWHM of the two Gaussian functions to be the same within a given galaxy. For the four galaxies with the highest quality spectra, we also show single Gaussian fits. Those yield significantly worse fits to the wings of the CO profiles, except for the face-on galaxy BzK-16000 that is consistent with a single Gaussian. Velocities are computed with respect to the tuning frequencies of the observations as listed in Table 1.

(A color version of this figure is available in the online journal.)

spectra show clear evidence for double-peaked emission profiles, suggestive of rotation. We obtained fits for all galaxies with a single Gaussian and with two Gaussian functions (in this case fixing the FWHM in each component to the same value). In most cases, we find that a fit with two Gaussian profiles provides a better description of the data. This includes objects like BzK-21000 and 17999 where, despite the fact that the evidence for a double peak profile is only tentative, a fit with a single Gaussian is disfavored as it is not able to accurately reproduce the rapid decrease of the flux at the edges of the spectra. In no case, we

Table 2
Observed Properties

Source	$z_{\rm Keck}$[a]	$z_{\rm CO}$	$v_{\rm CO}$ FWHM[b] (km s^{-1})	$I_{\rm CO[2-1]}$[b] (Jy km s^{-1})	S/N Det[c]	CO Size (kpc)	CO Blue/Red[d] (kpc)	P.A. Blue/Red	S(1.4 GHz) (μJy)
BzK-4171	1.465	1.46520 ± 0.00058	530 ± 32	0.65	8.3	11.3 ± 2.2	1.7 ± 1.7	...	34
BzK-21000	1.523	1.52133 ± 0.00036	444 ± 26	0.64	9.4	6.2 ± 1.9	5.3 ± 1.3	$-25 \pm 13^\circ$	43
BzK-16000	1.522	1.52496 ± 0.00028	194 ± 18	0.46	8.7	10.9 ± 2.9	...	...	19
BzK-17999	1.414	1.41385 ± 0.00032	440 ± 33	0.57	9.4	6.4 ± 1.9	5.7 ± 1.3	$-1 \pm 12^\circ$	34
BzK-12591	1.600	1.60019 ± 0.00076	$\sim$600	0.84	5.3	...	...	...	186
BzK-25536	1.459	1.45911 ± 0.00013	$\sim$170	0.36	6.4	...	...	...	28

Notes.
[a] The accuracy of Keck redshift is generally better than 0.001, except for BzK-16000 and 21000 (see Section 2.3).
[b] Derived from fitting double Gaussian profiles.
[c] To determine the S/N of the detection we add in quadrature the S/N from point source fitting of the data in each configuration, using the spectral regions with positive line emission (yellow regions in Figure 3).
[d] Spatial separation between the red and blue component in the CO[2–1] spectra.

do find evidence for continuum emission. We have combined all line-free channels in all galaxies to derive an average continuum at 3.3 mm of $< 100\,\mu$Jy at the 3σ level. This is consistent with the expectation, given the moderate SFRs in these galaxies (see Section 3), that the continuum emission should be at the level of 20–30 μJy.

Table 2 summarizes the results of the spectral fitting. Typical integrated CO[2–1] fluxes are 0.4–0.8 Jy km s^{-1}. The FWHM of the CO[2–1] emission is typically in the range of 400–600 km s^{-1}, with two notable exceptions: BzK-16000 and 25536. For BzK-16000, the narrower velocity range is most likely due to the fact that the galaxy is observed nearly face-on. For BzK-25536 this is likely, at least in part, due to the relatively low S/N of this source (see later in Section 6). The velocity centroid of the CO[2–1] emission can be used to derive a CO[2–1] redshift for the six galaxies. The CO redshifts agree well with the Keck redshifts to within $\Delta z = (z_{\rm CO} - z_{\rm Keck}) = 0.001$, the typical accuracies of the latter. Two objects show a larger offset: BzK-16000 has $\Delta z = 0.003$ that can be, at least partly, explained due to the lower accuracy of the Keck redshift. In this case, the optical redshift was determined through weak absorption lines in the UV rest frame (all other redshifts are from the detection of [O II]λ3727 emission lines); BzK-21000 has $\Delta z = -0.0017$, but its [O II] emission line is close to a very bright, telluric OH emission line.

2.4. Estimation of the Spatial Size of CO[2–1]

When comparing the D-configuration and B-configuration data (their respective *uv* coverages are shown in Figure 4), imaged separately, we find brighter peak flux densities in the D-configuration only data. This already indicates that the sources are spatially resolved. In order to quantitatively confirm this finding and to estimate the intrinsic size of the CO[2–1] emission, we have fitted models to the *uv* data. We have averaged the data over the spectral ranges showing positive emission (yellow-shaded regions in Figure 3). Given the modest S/N of the observations, we fitted circular Gaussian models to the data to limit the number of free parameters (four in this case: the spatial center R.A.–decl. positions, the total flux and the Gaussian FWHM). Figure 4 (right) shows the total CO[2–1] amplitude binned in ranges of *uv* distances, covering baselines from $\sim$ 50 m to $\sim$ 300–400 m. The overplotted model corresponds to the expected behavior in *uv* space of circular Gaussian profiles with the fitted sizes. In all four cases, we find that the sources are spatially resolved with a significance of $>3\sigma$ (5σ for BzK-4171). The FWHMs of the circular Gaussian functions range within 0.″7–1.″3, corresponding to 6–11 kpc at the redshifts of the galaxies.

2.5. Comparison to ACS Imaging

It is interesting to compare the CO[2–1] sizes to those from the *HST* imaging. In order to do that, we used the *Galfit* code (Peng et al. 2002) to characterize the ACS z-band images (F850LP filter), corresponding roughly to *U*-band rest frame. Table 3 summarizes the results of the Sérsic profile fitting. Preliminary results for the Sérsic profile fitting of BzK-21000 and 4171 were presented also in Daddi et al. (2008), and are consistent with the new measurements based on *HST* images that have twice the integration time (ACS GOODS release 2.0). Most of the sources are consistent with $n_{\rm Sersic} \lesssim 1.5$ profiles that are typical for spiral disks. For BzK-12591 and 16000, we find higher Sérsic indexes of 1.5 and 2. Inspection of the *HST* images (Figure 5) shows that these galaxies appear to be disk galaxies with a significant bulge component. We cannot exclude that bulges might exist in some of the other galaxies as well, and deep high-resolution near-IR observations (e.g., with WFC3 on *HST*) would be necessary to check this. Two galaxies have a Sérsic index lower than 1: BzK-17999 and 21000. For these two galaxies most of the UV light is concentrated in bright clumps, implying a light distribution flatter than an exponential. This is consistent with the appearance expected for gas-rich disks (Bournaud et al. 2008). We notice that in most cases the target BzK galaxies display a significant inclination in the ACS imaging, with axis ratios often below 0.5, i.e., they are not circularly symmetric. This implies that the size estimate derived from Sérsic model fitting might not be directly comparable with the cruder CO[2–1] sizes derived from (symmetric) circular Gaussian fitting. While it is not meaningful to fit our CO[2–1] observations with more complex spatial shapes due to the limited S/Ns, we decided to fit also the ACS images with circular Gaussian models to test for consistency between CO[2–1] and rest-frame UV sizes.

The results of this analysis are listed in Table 3. For three galaxies, the size measurements agree within 1σ–2σ. The exception is BzK-4171 for which the CO[2–1] size estimate is about three times larger than the UV rest-frame size, a difference significant at the 3.4σ level. This is also the object with the most accurate CO[2–1] size determination in our sample. If we average over the sample in order to increase the S/N, we find that the ratio of CO[2–1] to rest-frame UV sizes is 1.24 for all the four galaxies and 0.96 when excluding BzK-4171. Therefore, it

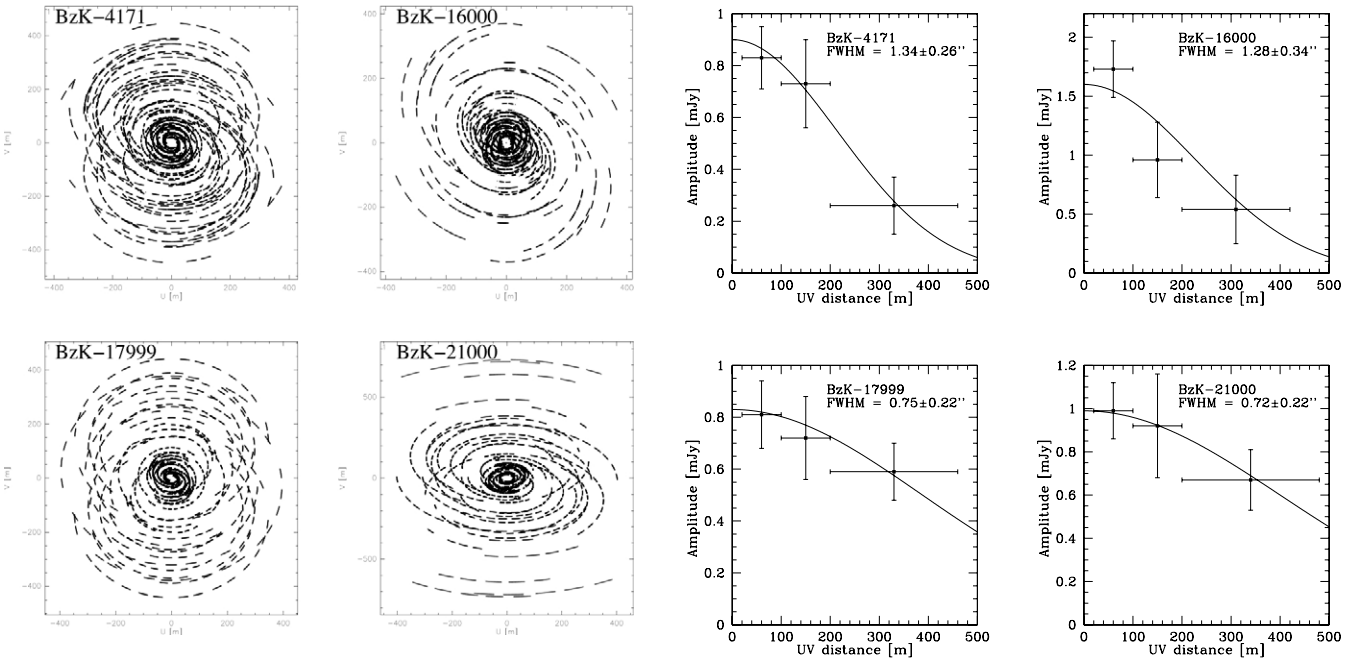

Figure 4. Left: *uv* coverage of the four target BzK galaxies that were observed also with the higher resolution B-configuration. Right: signal amplitude vs. baseline length in the *uv* plane. The solid curves show circular Gaussian models with FWHM as labeled. As a reminder, for a point/unresolved source the visibility amplitudes would be constant with *uv* distance.

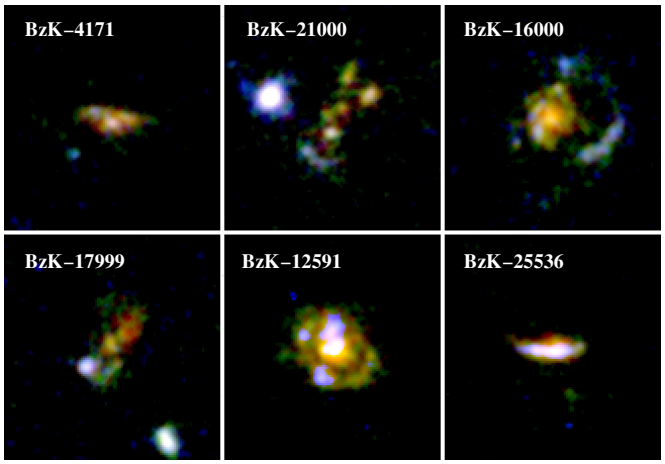

Figure 5. Three-color red giant branch (RGB) imaging of the six CO-detected BzK galaxies, based on ACS imaging of Giavalisco et al. (2004), release 2.0. Red is F850LP, green is F775W, and blue is F435W. We have used a two-pixel top-hat smoothing to improve the source visibility. Images are 3″ in size.

appears that CO[2–1] and rest-frame UV sizes are quite similar, within 20% on average.

2.6. Evidence for Rotation

We have analyzed the high-resolution CO[2–1] data of three of our galaxies (as one, BzK-16000, appears to be seen face-on) to check for signatures of rotation. Solid evidence for galactic rotation in near-IR-selected massive BzK galaxies has recently been derived using Hα observations from the SINS survey (e.g., Förster-Schreiber et al. 2009). Clearly, it would be important to confirm such findings based on the dynamics of the molecular gas that should trace the underlying velocity field.

In Figure 6, we show CO[2–1] contours imaged separately for the blue- and red-wing velocity ranges of BzK-4171, 21000, and 17999. For BzK-21000 and 17999, we observe a significant spatial displacement of the red (receding) versus blue (approaching) component. Their displacement is, not unexpectedly, aligned with the galaxy major axis as determined from the UV rest-frame observations. Also, the separation of the blue and red components is found to be quite consistent with the overall UV sizes of the galaxies. We conclude that we find evidence for galactic rotation in the disks in at least a couple of our sources.

Table 3
Rest-frame UV Morphology

Source	r_e (kpc)	n Sérsic	a/b	P.A.	FWHM$_{\rm circ}$ (kpc)
BzK-4171	3.7	1.0	0.40	86°	3.4
BzK-21000	6.2	0.5	0.37	−35°	11.0
BzK-16000	5.1	1.5	0.97	···	5.9
BzK-17999	4.7	0.5	0.42	−39°	7.7
BzK-12591	4.5	2.0	0.85	32°	6.0
BzK-25536	3.0	1.0	0.32	90°	3.4

Notes. The formal *Galfit* errors on the sizes and axis ratios correspond to an accuracy of better than 5%. The P.A. is measured east of north. FWHM$_{\rm circ}$ is derived from the fit of a circular Gaussian profile.

For a more direct assessment, we obtained position–velocity diagrams for our galaxies (Figure 7). In order to obtain sufficient S/N, we have binned the data over 100 km s^{-1} and extracted position–velocity diagrams using pseudoslits at the orientation defined by the major axis in the ACS imaging. As can be seen from Figure 7, we again find evidence for rotation. In particular, BzK-21000 shows the expected S-shaped structure indicative of disk rotation, consistent with a flat rotation curve. A less pronounced S-shaped rotation structure is also seen in BzK-17999.

In the case of BzK-4171, the approaching and receding parts of the emission are not significantly offset (Figure 6), and no clear evidence for rotation is present in the position–velocity

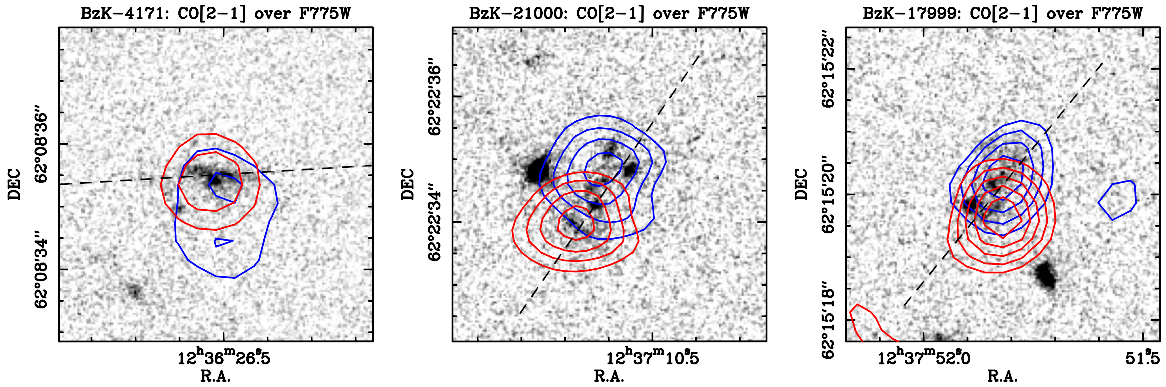

Figure 6. Contours of CO[2–1] are overlaid, separately for the blue (approaching) and red (receding) velocity ranges in the spectra, on ACS F775W images (5″ size). Contours start at $\pm 2\sigma$ and increase in steps of 1σ. The displacement of the red and blue parts of CO[2-1] for BzK–21000 and 17999 appears to be well aligned with the rest-frame UV major axis (dashed lines).

diagram. We explored position–velocity extractions at different orientations but could not find evidence for rotation at any position angle. We recall that for BzK-4171 we also got the puzzling result that the CO[2–1] size was found to be substantially larger than the rest-frame UV size. This object has the most pronounced double-horn profile in our sample, with a very significant central minimum reaching about 15% of the peak flux of the two symmetric horns. This galaxy is the most compact object in our sample in the rest-frame UV, and the half-light radius from the Sérsic fit is consistent within the limits with the spatial separation between the red and blue component. Higher resolution and higher S/N observations are required to constrain the rotation in the disk of BzK-4171.

3. GENERAL PROPERTIES OF THE SAMPLE

In this section, we discuss the overall properties of the CO-detected galaxies. We compare their colors, stellar mass, and SFRs to the full sample of near-IR-selected galaxies at similar redshifts to investigate whether they are representative galaxies for their mass. We further discuss the accurate derivation of the SFRs through multiwavelength indicators. We also explain the measurements of the stellar mass and stellar population parameters through fitting of synthetic models to the observed multicolor spectral energy distribution (SED).

3.1. Comparison to the Parent Sample

We have checked whether our source selection criteria (Section 2.1) imposed substantial biases on the choice of CO targets. Figure 8 shows the stellar mass–SFR diagram for the CO-detected galaxies in comparison with the full sample of BzK galaxies in GOODS-South. In the following, we use the GOODS-South sample for comparison even if the CO-detected galaxies are in the GOODS-N field as our GOODS-South catalog reaches 1.5 mag deeper in K, down to $K < 22$ Vega. In order to use the same estimators for all galaxies in this plot, we use the empirical relations by Daddi et al. (2004a) to estimate stellar masses and SFRs from UV luminosities in all objects (we discuss more accurate derivations of these quantities for the CO-detected galaxies below). From this plot, it appears that the targeted galaxies are massive, but that they lie right on top of the stellar mass–SFR correlation. The reason why they are massive systems is due to the fact that we required them to have a radio continuum detection: the typical 5σ limits of 20 μJy in our 1.4 GHz VLA maps (Morrison et al. 2010) correspond to SFRs of 66 $M_\odot$ yr^{-1} at $z = 1.4$ and SFR = 156 $M_\odot$ yr^{-1} at $z = 2.0$.

We note that the six galaxies in our sample are all at $1.4 < z < 1.6$; i.e., in the lower redshift range probed by the BzK selection that extends over $1.4 < z < 2.5$. This is due to the requirement of a radio detection coupled with the choice to observe the 2–1 transition of CO: such a transition has a rest-frame frequency of 230.538 GHz and can be observed with the PdBI only up to $z = 1.87$. We have chosen to observe the 2–1 transition rather than higher transitions in order to limit the uncertainties and corrections due to the possible presence of low-excitation molecular gas. Based on the results by Dannerbauer et al. (2009), we would have underestimated the total CO luminosity by a factor of ∼2.5 if we had observed the CO[3–2] transition and assumed constant brightness temperature in the CO emission. Observing CO[3–2] would have also resulted in substantially lower S/N for the galaxies in a fixed integration time, a finding consistent with the non-detection of similar galaxies in CO[3–2] by Tacconi et al. (2008) and Hatsukade et al. (2009).

Finally, we investigate if the requirement of the availability of a spectroscopic redshift prior to CO observations could have biased our sample. Given that most of the spectroscopic redshifts in GOODS-N were derived from optical spectroscopy, it is possible that this requirement might have biased our sample against optically faint galaxies or equivalently, given the near-IR selection of our sample, to objects with relatively low reddening by dust. Figure 9 shows the amount of reddening for the BzK galaxies, estimated from the slope of their UV continuum, plotted as a function of stellar mass. There is a clear trend between $E(B - V)$ and stellar mass in our sample, as reported also by Greggio et al. (2008). More massive galaxies are more strongly reddened, most likely a result of the mass–metallicity relation (Erb et al. 2006; Hayashi et al. 2009; Onodera et al. 2010). Incidentally, we note that the vast majority of galaxies with $M \gtrsim 10^{11}\ M_\odot$ (including the six CO-detected galaxies) are too red to be selected as BM/BX galaxies from the UV (Figure 9), a result consistent with what is found by van Dokkum et al. (2006) at slightly higher redshifts. From Figure 9 it is clear that the six CO-detected galaxies lie on the average trend of $E(B - V)$ versus stellar mass, i.e., they do not show particularly bluer colors than galaxies of similar stellar mass.

To summarize the characterization of our sample, we conclude that we have observed a subsample of BzK galaxies with fairly high stellar masses and toward the lower redshift range of the BzK selection but with overall physical properties (SFRs, stellar mass, and reddening) that are consistent with those of the general population of near-IR-selected galaxies at $z \sim 2$.

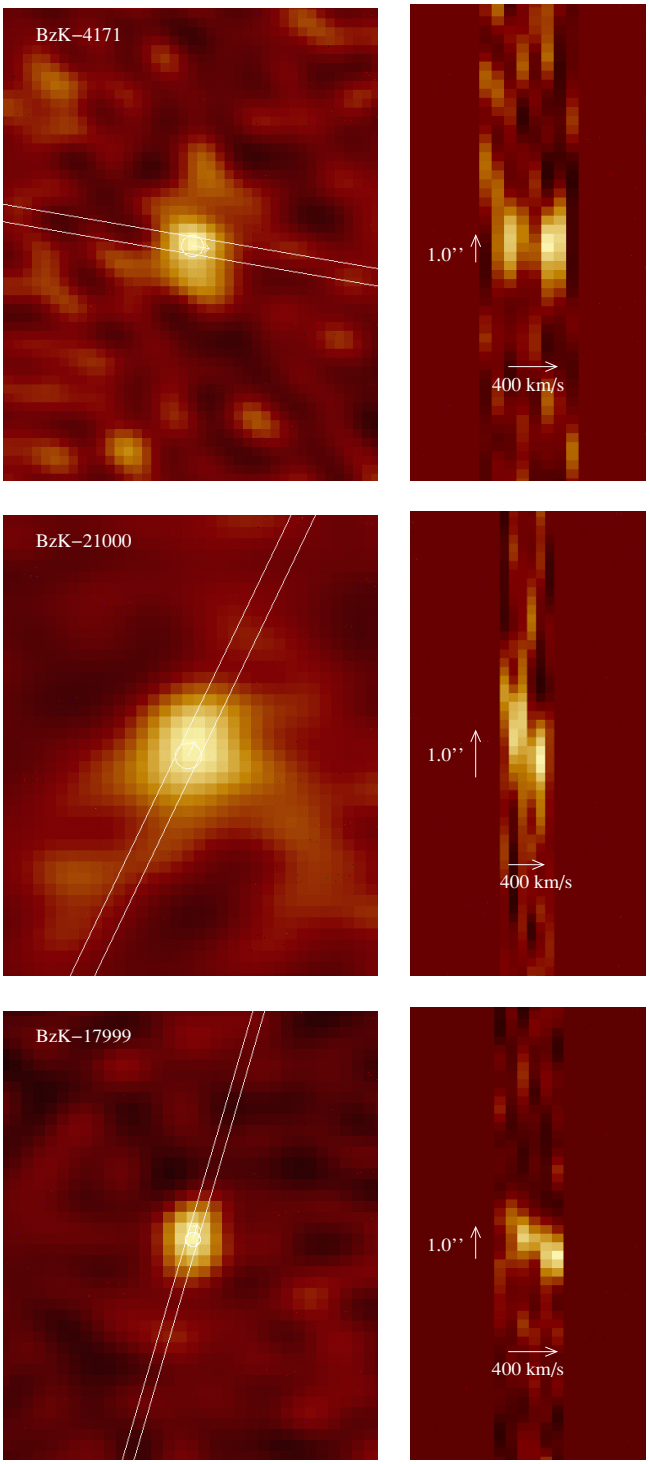

Figure 7. Left panels: CO[2–1] images with superimposed pseudoslits that are used to extract position–velocity diagrams. Right panels: the respective position–velocity diagrams. The arrow shows the spatial and velocity scales in the images (1″ corresponds to 8.5 kpc at $z = 1.5$). The data were binned in velocity (width: 100 km s^{-1}).

(A color version of this figure is available in the online journal.)

3.2. Total IR Luminosities and Star Formation Rates

In order to accurately derive the SFRs and IR luminosities of our sample galaxies, we have used all the available SFR indicators. This includes the dust corrected UV luminosities, mid-IR continuum luminosities from 24 μm *Spitzer* imaging and the VLA 1.4 GHz radio continuum. These data sets and

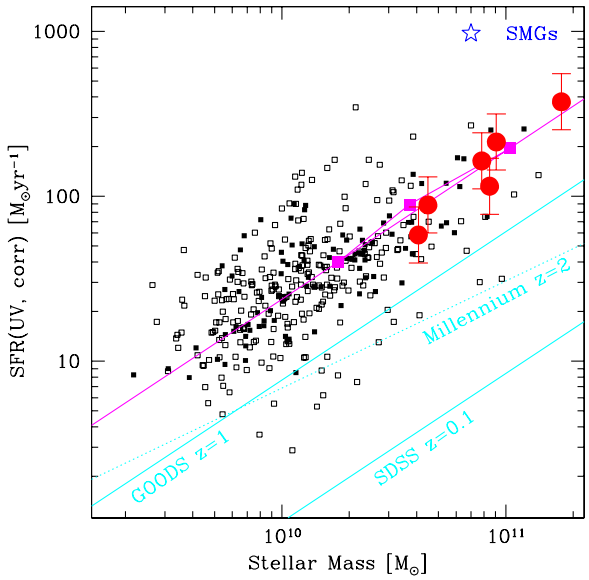

Figure 8. Location of the six BzK galaxies (large filled circles) in the stellar mass–SFR diagram. SFRs are derived from the UV luminosities at 1500 Å, corrected for dust reddening. We show typical error bars in the SFRs of the CO-detected galaxies based on the results in Section 3. The smaller points (squares; filled symbols are for spectroscopic redshifts, which are 30% of the sample) show individual BzK galaxies from the GOODS-South sample of Daddi et al. (2007a, 2007b) to probe smaller stellar masses (only star-forming BzK galaxies, or sBzKs, are shown). The magenta line shows the derived correlation between stellar mass and SFR. Filled magenta squares show the SFRs measured from radio stacking as a function of stellar mass (see also Pannella et al. 2009). The light blue lines with lower normalization show the same correlation at $z = 0.1$ and $z = 1$ (Elbaz et al. 2007) and in the Millennium simulations at $z = 2$ (dotted line). Figure adapted from Daddi et al. (2007a), but both SFRs and stellar masses were rescaled using a Chabrier IMF.

(A color version of this figure is available in the online journal.)

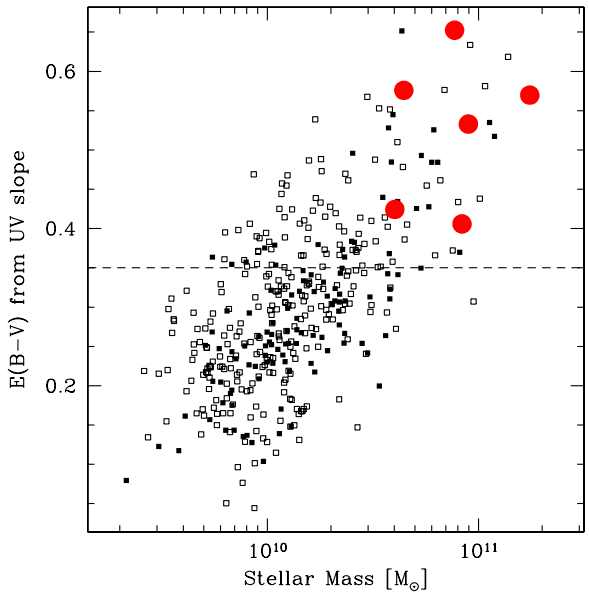

Figure 9. Reddening $E(B - V)$ estimated from the UV slope is plotted vs. the stellar mass. The large filled circles are the six CO-detected galaxies, while smaller symbols refer to the sample of near-IR-selected BzK galaxies (only star-forming BzK galaxies, or sBzKs, are shown). Objects above the horizontal dashed line are not selected with the BM/BX technique (Adelberger et al. 2004; Steidel et al. 2004).

(A color version of this figure is available in the online journal.)

the techniques that we use to convert observed luminosities into SFRs (and equivalently $L_{\rm IR}$; we adopt here $L_{\rm IR}/L_\odot =$

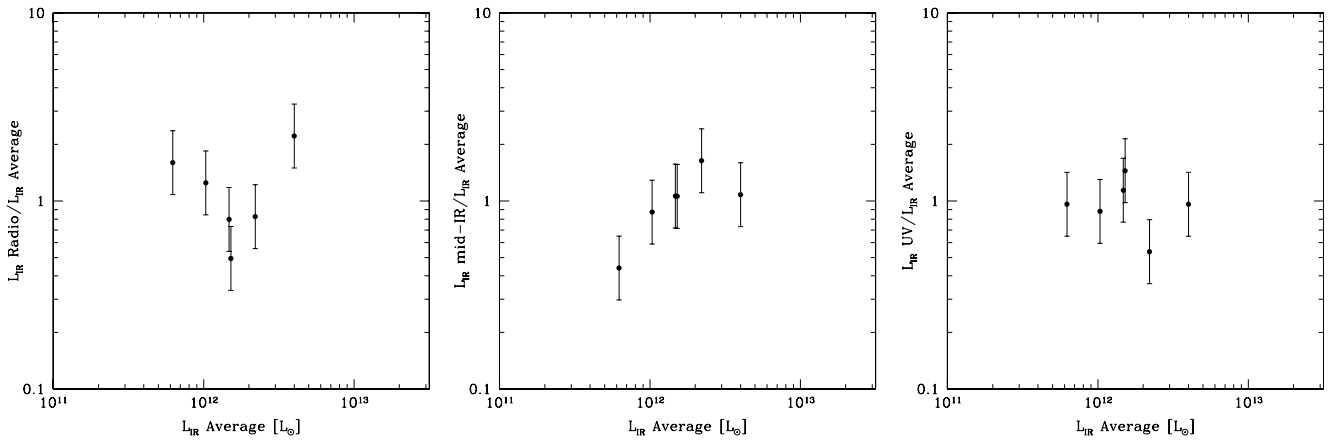

Figure 10. IR luminosities ($L_{\rm IR}$) for our galaxies were derived using three independent indicators: radio, UV, and mid-IR. We here compare the average of the three indicators for each source with the individual derivations for the radio (left panel), mid-IR (center panel), and UV (right panel). In each plot, we show a 0.17 dex error bar, corresponding to the scatter of all individual measurements with respect to their average. $L_{\rm IR}$ is a measure of the ongoing SFR in galaxies: we adopt $L_{\rm IR}/L_\odot = {\rm SFR}/[M_\odot\ {\rm yr}^{-1}] \times 10^{10}$, appropriate for a Chabrier (2003) IMF. From left to right in each panel, galaxy IDs are BzK-25536, 4171, 17999, 16000, 21000, and 12591.

Table 4
Physical Properties of the CO-detected Galaxies

Source	$\rm SFR_{best}$[a] ($M_\odot$ yr^{-1})	$L_{\rm IR}$[b] ($10^{12}\ L_\odot$)	$L'_{\rm CO}$[c] (10^{10} K km s^{-1} pc^2)	SFE ($L_\odot$ K^{-1} km^{-1} s pc^{-2})	$M_{\rm stars}$ ($10^{10}\ M_\odot$)	$M_{\rm gas}$[d] ($10^{10}\ M_\odot$)	$f_{\rm gas}$[e]	$M_{\rm dyn}$[f] ($10^{10}\ M_\odot$)	$\alpha_{\rm CO}$ ($M_\odot$ K^{-1} km^{-1} s pc^{-2})	$t_{\rm gas}$[g] (Gyr)	$t_{\rm rot}$[h] (Gyr)	$t_{\rm SFR}$[i] (Gyr)
BzK-4171	103	1.0	2.1	49	4.0	7.7	0.66	8.2	3.9 ± 1.2	0.74	0.09	0.39
BzK-21000	220	2.2	2.2	98	7.8	8.1	0.51	9.3	2.7 ± 1.4	0.37	0.17	0.36
BzK-16000	152	1.5	1.6	93	4.3	5.9	0.58	···	···	0.35	0.34	0.28
BzK-17999	148	1.5	1.7	85	3.9	6.3	0.62	7.3	4.0 ± 1.3	0.43	0.13	0.27
BzK-12591	400	4.0	3.2	124	11	12	0.52	···	···	0.29	0.09	0.27
BzK-25536	62	0.6	1.2	53	3.3	4.2	0.56	···	···	0.68	0.21	0.53

Notes.
[a] $\rm SFR_{best}$ is the average of dust corrected UV, mid-IR, and radio derived SFRs. Typical errors are at the level of 0.17 dex (see the text).
[b] We use $L_{\rm IR}/L_\odot = {\rm SFR}/[M_\odot\ {\rm yr}^{-1}] \times 10^{10}$, adapted from Kennicutt (1998) using a Chabrier IMF.
[c] We apply a correction of 16% to account for the CO[2–1] transition being slightly sub-thermally excited, Dannerbauer et al. (2009).
[d] Computed from $L'_{\rm CO}$, assuming $\alpha_{\rm CO} = 3.6$ as deduced from our observations.
[e] $f_{\rm gas} = M_{\rm gas}/(M_{\rm gas} + M_{\rm stars})$; the average error is 9% (including also the uncertainty on $\alpha_{\rm CO}$).
[f] Estimated for galaxies resolved in CO emission, except BzK-16000 that is seen nearly face-on; errors on $M_{\rm dyn}$ range from 30% to 50%.
[g] $t_{\rm gas} = M_{\rm gas}/{\rm SFR}$.
[h] $t_{\rm rot} = 2\pi r_e/(v_{\rm FWHM}/2)$ is the rotation time at the half-light radius.
[i] $t_{\rm SFR} = M_{\rm star}/{\rm SFR}$.

SFR/$[M_\odot\ {\rm yr}^{-1}] \times 10^{10}$, appropriate for a Chabrier 2003 IMF) are described in detail in Daddi et al. (2007a) and are largely based on the Chary & Elbaz template libraries (but we here use an improved 1.4 GHz map; Morrison et al. 2010). A comparison between these (and other) SFR indicators within the GOODS sample of BzK-selected galaxies for both individually detected sources and through stacked sources is discussed in detail in Daddi et al. (2007a) and shows that, on average, there is very good agreement between the different indicators.

We find that the SFRs estimated using the different techniques agree generally very well also for our CO-detected galaxies, typically to within much better than a factor of 2 (Figure 10). In particular, no galaxy in our sample would be classified as a mid-IR excess galaxy according to the classification of Daddi et al. (2007b), which could have suggested the presence of an obscured AGN. The largest discrepancy found is for BzK-12591 where we find a radio estimated IR luminosity that is twice as high as both the UV and mid-IR estimates. This might hint at a possible presence of an AGN, as also suggested by the possible [Ne v] emission in the optical spectrum.

We decided to adopt the average of the three estimators for the best measurement of $L_{\rm IR}$ and, subsequently, SFR, with the exception of BzK-12591 where we used the average of the UV and mid-IR estimates only (if we had included also the radio its SFR would have increased by 0.17 dex, leaving the remainder of our analysis basically unchanged). The uncertainty of this measure is derived using the dispersion of the differences between the average and each individual determination. From this we find that our SFR should be accurate to ∼0.17 dex. The SFRs derived from the UV (as used in Figure 8) agree with our best SFRs within 0.02 dex, with a scatter of 0.14 dex.

Inspection of the deep 70 μm imaging from the Far Infrared Deep Extragalactic Survey (FIDEL; Frayer et al. 2009) shows that BzK-21000 is detected with a flux of $4.9 \pm 0.7\ \mu$Jy, from the catalog of Magnelli et al. (2009), as noted also by Casey et al. (2009). The measured 70 μm flux corresponds to $L_{\rm IR} = 2.1 \pm 0.3 \times 10^{12}\ L_\odot$ using the Chary & Elbaz (2001) library that we adopt, in very good agreement with our estimate in Table 4. This is an independent confirmation of our $L_{\rm IR}$ and SFR estimates.

Overall, the galaxies in our CO sample are actively star forming, with SFRs ranging from about 6 $M_\odot$ yr^{-1} for BzK-25536 to 400 $M_\odot$ yr^{-1} for BzK-12591 (Table 4).

3.3. Stellar Masses from Synthetic Template Fitting

Multicolor photometry in the rest-frame UV, optical, and near-IR bands is available for our CO-detected galaxies in GOODS-N, as presented by Daddi et al. (2007a). The

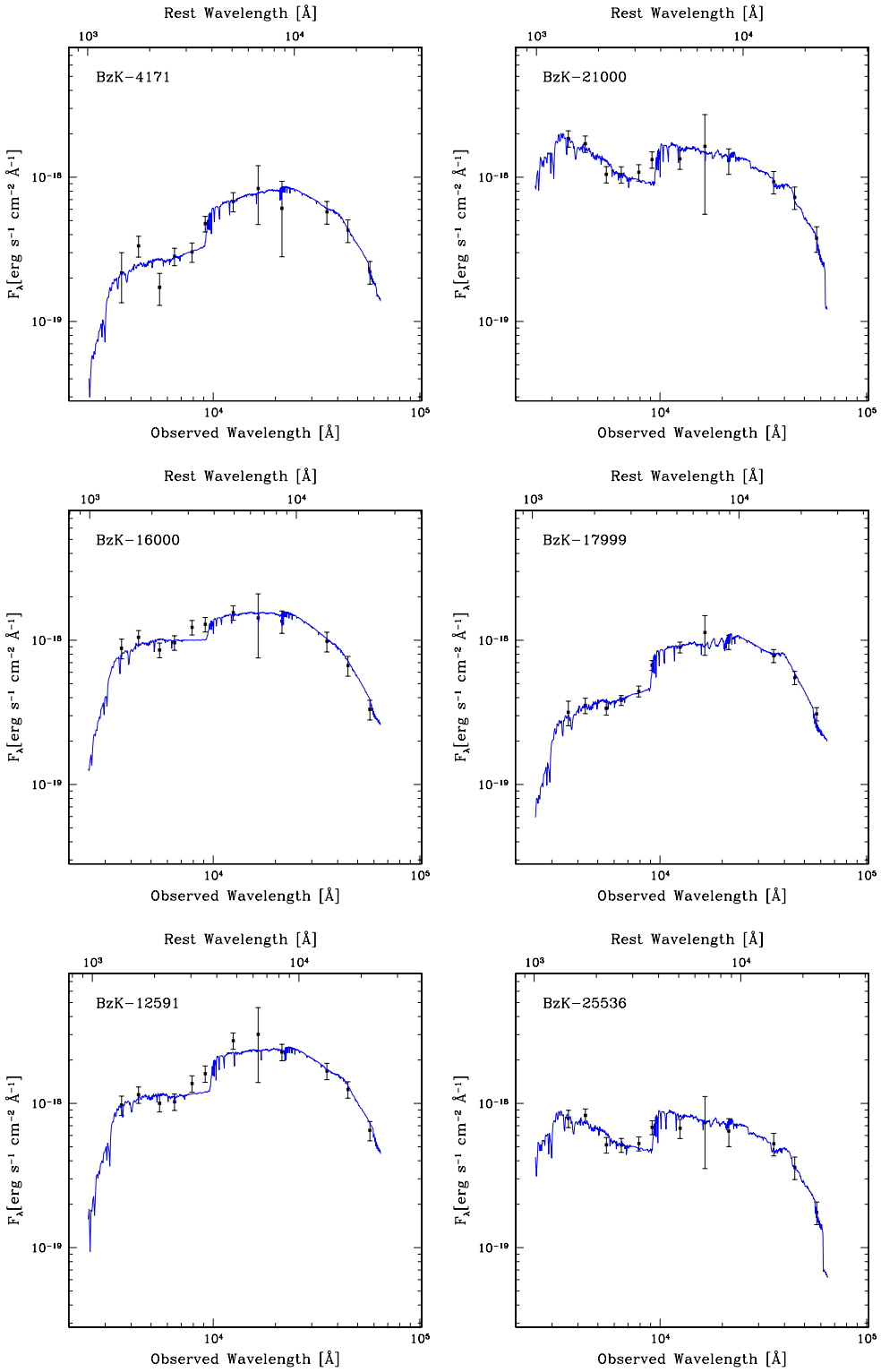

Figure 11. Spectral energy distribution of our target sources showing best-fitting synthetic templates from the M05 library. We consider constant star formation rate models with 0.5, 1, and 2 solar metallicities and allow for reddening using a Calzetti et al. (2000) law. Errors bars in the plots have been increased to formally have $\chi^2_{\rm reduced} = 1$.

(A color version of this figure is available in the online journal.)

UBVRIzJHK photometry, plus the photometry in the first three IRAC bands at 3.6 μm, 4.5 μm, and 5.8 μm is shown for all target galaxies in Figure 11.[10]

We used synthetic templates from the library of Maraston (2005) to derive stellar population properties and in particular stellar masses. These templates have a consistent treatment of the emission of AGB stars that is important for the correct derivation of stellar masses in the distant universe (see, e.g., Maraston et al. 2006). Given that all of the galaxies in our sample

[10] Following Maraston et al. (2006) and other work, we do not use the IRAC 8.0 μm band as it appears to be often contaminated by dust emission in the BzK galaxies; see also Daddi et al. (2007b).

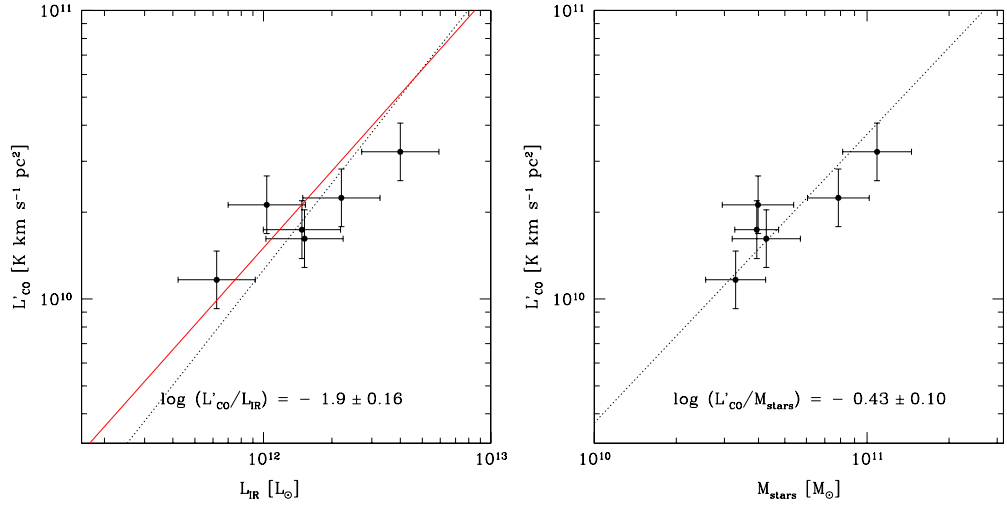

Figure 12. CO luminosities ($L'_{\rm CO}$) vs. the bolometric IR luminosities ($L_{\rm IR}$, left panel) and vs. the stellar masses (right panel). The dotted line in each panel is the best linear fit. The average ratio and dispersion is reported in the bottom of each panel (units are K km s^{-1} pc^2 $L_\odot^{-1}$ for the ratio in the left panel and K km s^{-1} pc^2 $M_\odot^{-1}$ in the right panel). The red solid line in the left panel corresponds to the fit to BzK galaxies at $z = 1.5$ and spiral galaxies, as shown in the left panel of Figure 13. In both panels galaxy IDs are, from top to bottom: BzK-12591, 21000, 4171, 17999, 16000, and 25536.

(A color version of this figure is available in the online journal.)

are actively star forming, we have used templates with a constant SFR, a large range of ages, Chabrier (2003) IMF and a range of metallicities (half solar, solar, and twice solar, appropriate for the expected range in stellar masses). We allow for reddening using the Calzetti et al. (2000) extinction law. We explicitly account for the mass loss due to stellar evolution, so that the stellar masses that we derive are lower by some 10%–20% (depending on age; see Figure 3 of Maraston et al. 2006) than the time integral of the SFR. The results are summarized in Table 4. The stellar masses range from 3.3×10^{10} $M_\odot$ for BzK-25536 to 1.1×10^{11} $M_\odot$ for BzK-25536. The fitted stellar masses are only 0.06 dex lower on average than those from the D04 empirical formula, with a scatter of 0.08 dex. This implies that Figure 8 is relevant also for the stellar masses.

We estimated the uncertainties in the derivation of the stellar masses on the basis of χ^2 variations, following Avni (1976) for the case of one interesting parameter, marginalizing thus on the template age, reddening, and metallicity. We find that, given our accurate multiwavelength SEDs, the formal (statistics) 1σ error on the stellar masses are of order of 0.10–0.15 dex.

4. STAR FORMATION EFFICIENCIES

From the observed CO[2–1] fluxes, we have derived CO luminosities $L'_{\rm CO}$ spanning a range of $(1.2–3.2)\times10^{10}$ K km s^{-1} pc^2 (Table 4; see Solomon & Vanden Bout 2005 for the conversion formula in the adopted units). We here have applied a 16% correction to convert luminosities derived from CO[2–1] to $L'_{\rm CO}$ (defined relative to the fundamental CO[1–0] transition) based on the BzK excitation results in Dannerbauer et al. (2009). Given the flux measurement errors and the uncertainty in this conversion, we estimate typical errors in $L'_{\rm CO}$ to be at the level of 0.1 dex.

We compare the CO luminosities to the *I R* luminosities and stellar masses of our sample galaxies in Figure 12. We find that the CO emission correlates well with both $L_{\rm IR}$ (hence SFR) and stellar mass (we exclude at the 2.5σ [3σ] confidence level that the CO emission does not correlate with SFR [mass]). The ratio of $L'_{\rm CO}/L_{\rm IR}$ (i.e., SFE) has a scatter of only 0.16 dex, while the individual values are all within a factor of 2.5. The scatter is in fact similar to the error of $L_{\rm IR}$ only, which possibly dominates the total error (this would suggest even lower intrinsic scatter in $L_{\rm IR}/\ L'_{\rm CO}$). The ratio of $L'_{\rm CO}/M_{\rm stars}$ has an even lower scatter of 0.10 dex. This is driven by the fact that the formal errors on stellar masses are lower than those on IR luminosities. This correlation of the CO luminosity with *both* the SFR and stellar mass is not surprising, given that the six galaxies lie on top of the stellar mass–SFR correlation and their SSFR has a scatter of only 0.12 dex. However, it is remarkable that we can now probe for the first time that the narrow range of SSFR corresponds to a similarly narrow range of SFEs, i.e., is directly related to the gas properties.

In Figure 13, we compare the CO and IR luminosities of the six CO-detected BzK galaxies with other cosmologically relevant galaxy populations: SMGs (Greve et al. 2005; to which we add more recent results of Daddi et al. 2009a, 2009b and Frayer et al. 2008), quasars (QSOs; Riechers et al. 2006; Solomon & Vanden Bout 2005), local ULIRGs (Solomon et al. 1997), and local spirals taken from the HERACLES survey (Leroy et al. 2008, 2009) and from the Virgo Cluster survey of Wilson et al. (2009). We notice that in Daddi et al. (2008) we used the results of Yao et al. (2003) to define a bona fide comparison sample of local spirals, following Solomon & Vanden Bout (2005) and Greve et al. (2005). While the results and conclusions of this paper would remain the same if we were still using the Yao et al. (2003) sample, we here prefer the more recent samples as the Yao et al. sample was selected in the submillimeter. Also, we here chose not to adopt the IR luminosities for SMGs estimated by Greve et al. (2005) but use a lower conversion factor between 850 μm flux and IR luminosity to account for the evidence that their SEDs are colder than previously thought (e.g., Pope et al. 2006, 2008; Kovács et al. 2006; Daddi et al. 2009b). In addition, we exclude lower luminosity objects from the Solomon et al. (1997) sample requiring $L_{\rm IR} > 0.7 \times 10^{12}$ to obtain a sample of ultra-luminous IR galaxies with IR luminosities similar to the BzK galaxies.

Based on our sample of six galaxies, we thus confirm and extend the result of Daddi et al. (2008) that the typical SFE of massive BzK galaxies is similar to that of spirals and significantly lower than that of SMGs. We find that the average

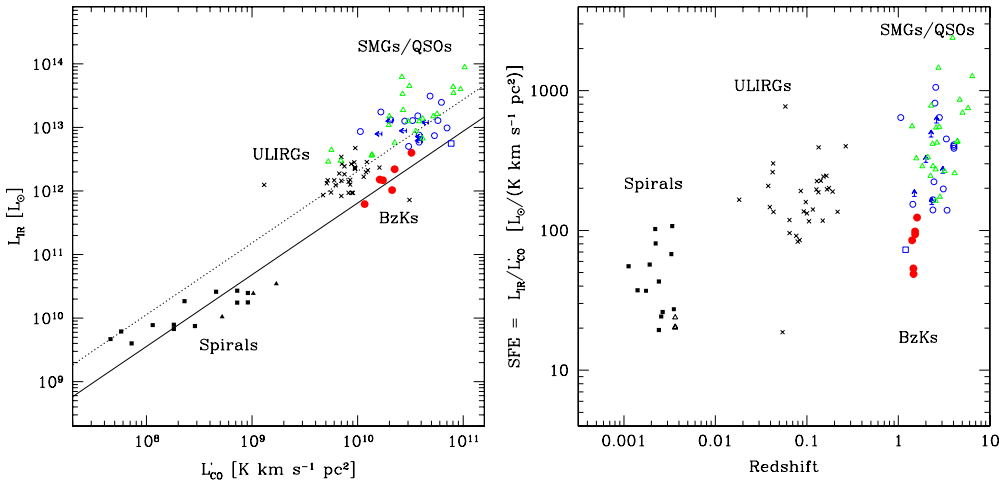

Figure 13. Comparison of the CO and IR luminosities of the CO-detected BzK galaxies (red filled circles) to various local and distant samples: SMGs (Greve et al. 2005 and Daddi et al. 2009a, 2009b: blue empty circles; Frayer et al. 2008: blue empty square), QSOs (Riechers et al. 2006; Solomon & Vanden Bout 2005; green empty triangles), local ULIRGs (Solomon et al. 1997: crosses), local spirals (Leroy et al. 2008, 2009: filled squares; Wilson et al. 2009: filled triangles). For local spirals, we associate a Hubble-flow redshift (right panel) based on the actual distance. The solid line in the left panel shows the best-fitting L'_{CO} vs. L_{IR} relation to the combined sample of local spirals and distant BzK galaxies. The dotted line shows the same relation with normalization higher by 0.5 dex.

SFE (in units of $L_\odot$ K^{-1} km^{-1} s pc^{-2}; the errors given in the following are the uncertainties of the mean) of BzK galaxies is 84 ± 12, that of SMGs is 390 ± 60, for QSOs we find 590 ± 100, for local ULIRGs we have 250 ± 30, and local spirals have 48 ± 7. Therefore, the typical BzK galaxy has about 80% higher SFE of that of a local spiral, but individual values are well within the range measured for local spirals even though BzKs are a hundred times more luminous. Local ULIRGs have SFEs that are three times larger on average than BzK galaxies. Although there is some overlap in the spread of individual targets, one can see that the two distributions do not really overlap in the L_{IR} versus L'_{CO} plane (Figure 13).

For SMGs/QSOs, the average SFE is 4.5/7 times larger than that of an average BzK galaxy. Although at least one case is known of an SMG with a SFE at the level of that of BzK galaxies (Frayer et al. 2008), for the vast majority of the sample the distribution of values are fairly disjoint. We note that, in contrary to our BzK galaxies, the CO luminosities of SMGs are derived from high-J transitions, and could be underestimated if a substantial amount of cold gas is present. Such a correction could indeed be important in some cases (Greve et al. 2003; Carilli et al. 2010) but the difference still appears to be quite significant if a correction was applied using the average CO SEDs of SMGs (Weiß et al. 2005, 2007) or local ULIRGs (Papadopoulos et al. 2007).

Given the comparable SFE of local spirals and BzK galaxies, and the evidence that indeed the BzK galaxies are gas-rich disks in the distant universe, we can formally consider them as a homogeneous population and derive the best-fitting L'_{CO} versus L_{IR} relation for the combined population. We find the relation

$$\log(L_{IR}) = 1.13 \times (\log L'_{CO}) + 0.53, \quad (1)$$

with L'_{CO} in units of K km s^{-1} pc^2 and L_{IR} in units of $L_\odot$. Both parameters in the fit are determined with an accuracy of 0.07. The relation appears to fit both the sample of BzK galaxies (see also Figure 12) and local spirals well, with a root mean square scatter of 0.24 dex. The local ULIRGs and SMGs are systematically offset from the fit, but are consistent with a relation having a similar slope but with a factor of 3–4 higher normalization.

Similarly, Figure 13 shows that our BzK galaxies should have been factors of 3–4 fainter in their CO fluxes had they followed the trends previously established for equivalently luminous galaxies such as local ULIRGs and SMGs, as discussed in the introduction. Had that been the case, it would have taken $\gtrsim$10 times longer integrations to detect these sources, which would have made detections impossible until ALMA is in full operation.

5. GAS KINEMATICS IN CLUMPY DISKS: NUMERICAL SIMULATIONS

A critical piece of information that our observations can provide is the derivation of the dynamical mass of the systems through the observed gas kinematics and spatial extent. In today's disk galaxies, the cold gas component is slowly rotating and directly traces the dynamical mass, which relates to the circular velocity squared and the radius of the system (e.g., de Blok et al. 2008). However, gas motions in high-redshift disk galaxies are more complex. In particular, larger molecular gas reservoirs are present and optical morphologies are dominated by giant star-forming clumps. This is seen in our sample (Figure 5) as well as in the majority of star-forming disks at high redshift (Elmegreen et al. 2007). These giant clumps are up to $\sim$1000$\times$ more massive than the star-forming clouds of today's spirals (Elmegreen et al. 2009b). Such gas-rich clumpy disks can have significant non-circular motions (Immeli et al. 2004; Bournaud et al. 2008) and show strong turbulence in their ionized gas (e.g., Genzel et al. 2008; Förster-Schreiber et al. 2009). It is likely that such motions are also present in their cold gas (CO) component (Bournaud & Elmegreen 2009; Dekel et al. 2009a). Clumpiness and turbulence influence the kinematics, sizes, velocity fields, and dynamical mass estimates of distant galaxies (Bournaud et al. 2008; Burkert et al. 2009).

To recover dynamical masses accurately from CO velocities and to estimate associated uncertainties, we used numerical simulations of gas-rich clumpy galaxies based on the work of Bournaud et al. (2007, hereafter BEE07). These simulations start as gas-rich, gravitationally unstable disks that rapidly evolve into clumpy disks with a phase space distribution similar to cosmological simulations of clumpy disk formation (Agertz

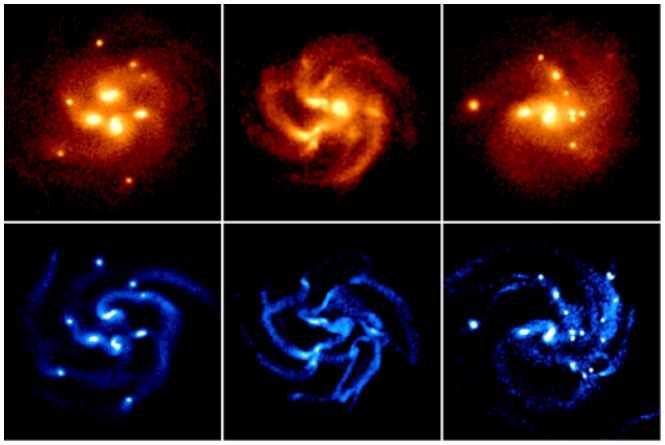

Figure 14. Few examples of our simulations of clumpy disk galaxies, based on the results of Bournaud et al. (2007). Top panels show the distribution of stellar light as observed in the UV (tracing mainly star formation), bottom panels that of the molecular gas. The distribution of star formation and optical morphologies are dominated by giant clumps, and our models include a variety of clumpiness and bulge fractions consistent with observed star-forming disks at high redshift. These snapshot show a 40 × 40 kpc area (5″ × 5″ at $z = 1.5$).

(A color version of this figure is available in the online journal.)

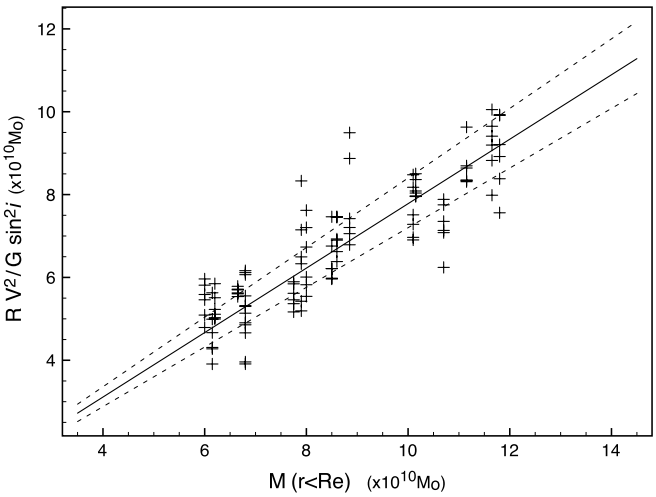

Figure 15. Calibration of the relation between the $R \times V^2$ estimator corrected for inclination effects (y-axis) and the effective amount of mass contained within the half-light radius (r_e, x-axis), based on clumpy disk models. Sequences of points at fixed dynamical mass correspond to the same model observed with different inclinations and azimuths. The solid and dashed lines show the best-fitting relation (Equation (2)) and the 1σ scatter on the relation, respectively.

et al. 2009; Ceverino et al. 2010) and consistent with observed clumpy galaxies (see BEE07; Bournaud et al. 2008). The initial conditions ($t = 0$) of the six new models used here were scaled to match the typical masses and sizes of the observed galaxy sample, and are as follows: stellar masses of 6×10^{10} $M_\odot$, initial half mass radii of 5 kpc, gas fractions $f_g = (M_{gas}/M_{gas}+M_{stars})$ of 30%, 50%, and 70%, and dark matter fractions $f_{DM} = (M_{dark}/(M_{dark} + M_{gas} + M_{stars})$ of 15% and 35% within the effective radius. The output of the simulations were retained after 250, 450, and 650 Myr, which, in the evolutionary sequence studied in BEE07, covers all stages from very clumpy bulgeless morphologies to smoother bulgy systems, consistent with our observed sample (Figure 14; compare to Figure 5). In each case, the system was *observed* with 30° and 60° inclinations and at three different azimuths, giving a total of 108 "independent" projections.

Taking advantage of the fact that the actual mass encompassed at the effective radius r_e can be directly measured in the simulations, we compare its value to a crude estimate of the dynamical mass, $(v_{FWHM}/2)^2 \times r_e/(G\ \sin^2 i)$, in order to derive a robust method to estimate dynamical masses from high-redshift CO spectra. For each projection of the simulations, we derive the spatial distribution of "molecular" gas component. To do so, we only consider gas in regions where the density is higher than 100 atoms cm^{-3}.[11] We measure the effective radius r_e not as the true half-light radius but as the effective radius of a Sérsic fit to the radial profile distribution, just as in our observations. We derive synthetic CO spectra from which we estimate the FWHM velocity v_{FWHM}. We also produce UV stellar images from the simulations to reproduce deprojection uncertainties and compare UV and CO sizes (see below). In this way, the $(v_{FWHM}/2)^2 \times r_e/(G\ \sin^2 i)$ ratio is computed with the same definitions, assumptions, and possibly biases as in the observations. The main result of this exercise is shown in Figure 15. We find the following best-fitting relation to the actual mass inside r_e:

$$M(r < r_e) = 1.3 \times \frac{r_e \times (v_{FWHM}/2)^2}{G\ \sin^2 i} \pm 12.5\%. \qquad (2)$$

The *correction factor* of 1.3 includes various effects.

1. The flattening of the baryonic mass distribution in a disk (Binney & Tremaine 2008). This has a small effect (around −5%) on the total (+30%) correction factor.
2. A possible bias on estimating the projection angle i because of the clumpiness of these galaxies. We deprojected simulated UV images just like observations, so that any uncertainty and bias on i are included in our results (Equation (2) and the scatter of Figure 15). We actually found that the inclination i retrieved from the UV images tends to slightly overestimate[12] the actual projection angle (which is known in simulations). This is also a small effect, around +10% on $M(r < r_e)$.
3. The fact that gas motions largely differ from circular orbits is the main effect, around +25% on $M(r < r_e)$. The giant and massive gas clumps interact with each other, undergo dynamical friction and migrate radially (BEE07; Dekel et al. 2009a). The presence of a high velocity dispersion σ decreases the observed rotation velocity v_{rot} compared to the actual circular velocity v_{circ} tracing the potential, with $v_{circ}^2 \simeq v_{rot}^2 + 3\sigma^2$, where σ is the one-dimensional gas velocity dispersion (observed line-of-sight dispersion) and the factor 3 is for isotropic gas turbulence in three dimensions. The effect is also known as "asymmetric drift" in stellar kinematics, and the equivalent of a turbulent pressure support in addition to the rotational support for a gas disk (Burkert et al. 2009; Elmegreen & Burkert 2010). The velocity dispersion σ of the CO component cannot be directly measured given the current observations, but should

[11] This selection actually includes almost all the gas mass in the models, since the gas fraction is high and the density is high almost everywhere.

[12] For instance, a face-on disk ($i = 0$) could have a large fraction of its light distributed in a few main clumps, leading to an axis ratio $b/a < 1$ and hence a derived inclination $i > 0$.

be several tens of km s^{-1} based on Hα data (e.g., Förster-Schreiber et al. 2009) and observed clump sizes (which is set by the Jeans mass; Bournaud & Elmegreen 2009). The theoretical correction factor for the mass expected from a disk with a circular velocity of about 200 km s^{-1} is then consistent with the +25% correction from our simulations.

Our simulations also have the advantage of including the clumpiness of the gas resulting from an irregular sampling of the underlying velocity field and a dispersion in the dynamical mass measurements—a given model has different velocity widths $v_{\rm FWHM}$ when we observe it from different azimuths. The resulting uncertainty on the estimated mass is nevertheless relatively small, about 12.5% (this uncertainty accounts for the method used and clumpiness of disks). In summary, the presence of giant clumps does not significantly hamper the possibility to estimate accurate dynamical masses.

The models were started with similar gas and stellar sizes, and we checked that the half-light radii derived from the UV stellar emission and from the CO emission remain similar during the evolution (Figure 14). This is in agreement with what is found for our sources (see Section 2) as well as local disks (Leroy et al. 2008). This implies that, referring to the dynamical mass within the half-light radius, the quantity computed according to Equation (2) should be compared to *half* of the total amount of stellar mass and gas mass in the system, plus the amount of dark matter eventually present within r_e, i.e.,

$$M(r < r_e) = 0.5 \times (M_{\rm star} + M_{\rm gas}) + M_{\rm dark}(r < r_e). \quad (3)$$

Applying this result to observations, we derive $M(r < r_e)$ from Equation (2), subtract the known stellar mass $M_{\rm star,tot}$ and an estimate of $M_{\rm dark}(r < r_e)$ to finally derive the gas mass $M_{\rm gas,tot}$ and compare to the observed CO fluxes.

Note that we calibrated the measurements (Equation (2) and Figure 15) at a radius $r = r_e$ and using the $v_{\rm FWHM}$ velocity, in order to match observational measurements. Dynamical masses estimates at different radii should be similar, as the main contribution to these factors in Equation (2), namely, clumpiness and high turbulence, are present all over high-redshift disks.

The numerical simulations spanned gas fractions from 30% to 70%. Reproducing clumpy structures similar to those observed (Figures 5 and 2) requires high gas fractions and disk masses (Bournaud & Elmegreen 2009), and we will show that our observations support a high molecular gas fraction in these galaxies. In any case, kpc-sized clumps are observed, which imply a large Jeans length and a high turbulent speed (velocity dispersion). As the underlying physics in Equation (2) is based on the gas velocity dispersion, it should remain valid independent of the actual gas fraction.

5.1. Explaining the Shapes of the Observed CO Spectra

An application of the numerical models is to produce synthetic CO spectra and compare their shapes to the observed ones. Indeed, the observed spectra have some particularities that would not be expected for regularly rotating disks such as seen in $z = 0$ spirals.

For example, the CO spectrum of BzK-4171 (Figure 3) has a very marked and quite symmetric double-horn profile with a pronounced central depression in the center, falling to only 15% of the peak flux. Gas spectra in local galaxies show double-horn profiles but the emission at zero velocity never falls below 50% of the peaks (e.g., Walter et al. 2008). The observed feature in BzK-4171 cannot be easily explained by assuming

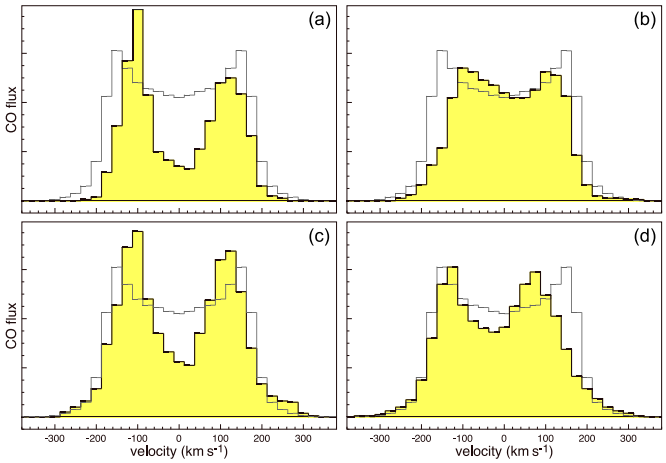

Figure 16. Four CO spectra extracted from our simulations. The gray histogram shows the initial ($t = 0$) uniform disk, the black lines and yellow histograms correspond to evolved stages in the simulations (i.e., realistic clumpy disks). Because of the discrete sampling of the velocity field related to the clumpiness of the gas, and the individual motions of each clump, the predicted spectra are more irregular than for $z = 0$ spiral galaxies. Overall, the typical double-horn profile is preserved, but there can be a strong central dip at zero velocity ((a) and (c), resembling the observed spectrum of BzK-4171 in Figure 3) or, on the other hand, relatively flat spectra with little zero-velocity central depression ((b), as in BzK-17999). Asymmetrical spectra ((a) and (d)) are also found, as observed in BzK-12591 and BzK-25536. The velocity width of these spectra is smaller than for the initial smooth rotating disk. This corresponds to clump evolution and migration with rotation velocities below the circular velocity, and the associated turbulent pressure support that compensates for the lack of rotation. This lies at the origin of the calibration factor in Equation (2).

(A color version of this figure is available in the online journal.)

that the molecular gas is in a ring: removing molecular gas from the system barycenter would still leave substantial amount of emission at zero velocity, coming from regions where the gas rotation velocity is perpendicular to the line of sight. For instance, even a pure thin ring rotating with $V/\sigma = 10$ would have a zero-velocity emission at 42% of the peaks. Figure 3 shows that also BzK-12591 and BzK-25536 have significantly asymmetric spectra, with a flux in one horn much higher than in the other horn. The spectrum of BzK-17999 is almost flat around the central velocity.

The synthetic CO spectra from our numerical simulations shed light on this situation. Spectra qualitatively similar to BzK-4171 are found, as well as spectra where the zero-velocity level is quite high, and double-horn profiles that are strongly asymmetric (Figure 16). The explanation is that much of the CO emission comes from a few big clumps, and therefore is *discretized*. At particular projections, there can be a lack (or an excess) of zero-velocity emission, when few (many) clumps have velocities perpendicular to the line of sight. Significant asymmetries arise when the clumps are not uniformly distributed between the blueshifted and redshifted parts of the disk.

The successful reproduction of the observed spectra give confidence that our models are correct, at least to first order. More generally, both observations and modeling show that turbulent and clumpy disks at high redshift can have integrated spectra that are distinct from what is seen in the local universe.

An interesting characteristic in the simulated spectra is that, in spite of their disturbed shapes, the velocity spread remains about the same in the two horns (red- and blueshifted sides). One of the two sides can have a much higher flux, but not a much larger velocity spread. This is seen also in the observed spectra.

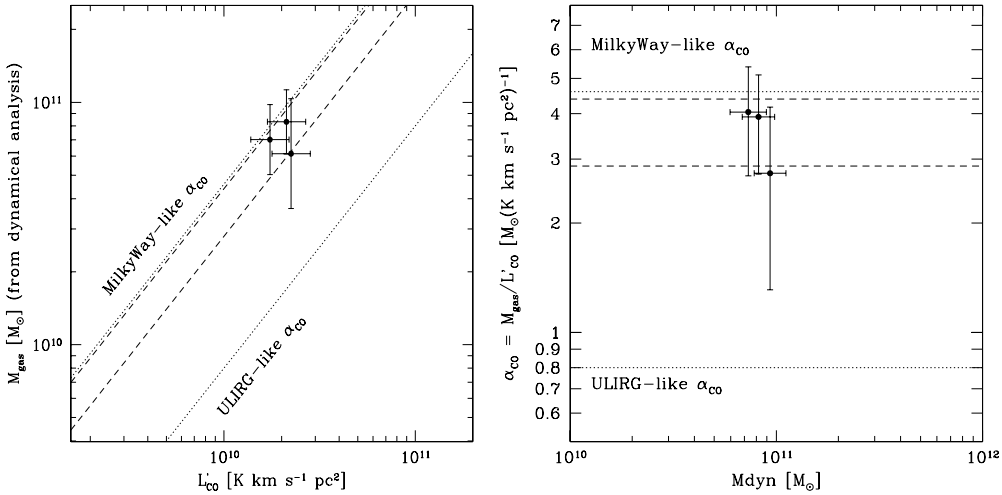

Figure 17. Constraints on the CO luminosity-to-gas mass conversion factor (α_{CO}). The analysis was possible for three galaxies for which we plot gas masses vs. CO luminosities (left panel) and their ratio (α_{CO}) vs. the dynamical masses (right panel). The dashed lines show the 1σ range on α_{CO} derived by combining the measurements for the three galaxies. The dotted lines show the conversion factor for the Milky Way galaxy (top) and for local ULIRGs (bottom). From left to right galaxies are BzK-17999, 4171, and 21000.

6. ESTIMATING GAS MASSES IN NORMAL HIGH-REDSHIFT MASSIVE GALAXIES

Based on the results shown in Figure 15 and using Equations (2) and (3), we proceed to estimate the dynamical mass within r_e of the CO-detected BzK galaxies, based on the v_{FWHM} velocity from CO[2–1] spectra, the stellar half-light radius (that corresponds to the CO half-light radius), and the inclination i derived from the b/a axis ratio seen in the ACS imaging. Values and uncertainties are given in Tables 2 and 3. We limit our analysis to the CO-detected galaxies that were resolved in CO. We did not estimate a dynamical mass for BzK-16000 because the correction due to its inclination is quite uncertain ($b/a \simeq 1$).

In order to estimate the gas mass following Equation (3), we account for a dark matter fraction within r_e of 25% (see also next section). Disk galaxies are known to be dominated, at their effective radius, by baryons more than by dark matter (Bosma 1981; de Blok et al. 2008; Trachternach et al. 2008—dark matter dominates rotation curves only at much larger radii). This implies that the dark matter fraction is *well below* 50%, and there is no expectation for a major change with redshift (see also Förster-Schreiber et al. 2009). The structural properties of $z \sim 2$ galaxies also indicate that, within their visible, star-forming extent, they have baryonic masses and disk masses that should account for at least two-thirds of the total masses (e.g., Bournaud & Elmegreen 2009).

We find dynamical masses within r_e for the three galaxies in the range of $(7–9)\times10^{10}\,M_\odot$ with typical uncertainties at the level of 30%. Subtracting the stellar and dark mass from the dynamical mass (Equation (3)), we derive a total gas mass of order $(6.1–8.3)\times10^{10}\,M_\odot$ for the three galaxies. After propagating all the estimated uncertainties in our measurements and adding in quadrature the 12.5% uncertainty associated to Equation (2), the uncertainty in the total gas mass estimate is about 30% for BzK-4171 and 17999 and 50% for BzK-21000.

These gas mass estimates are derived independently from the observed CO luminosities. Thus, taking the ratio of the gas mass estimates and the CO luminosities, we can derive a conversion factor $\alpha_{CO} = M_{gas}/L'_{CO}$ for each system (see Table 4 and Figure 17), and find a combined result of

$$\alpha_{CO} = 3.6 \pm 0.8\,M_\odot(\mathrm{K\ km\ s^{-1}pc^2})^{-1}. \quad (4)$$

Although the uncertainty in the individual α_{CO} estimates is significant, their α_{CO} values are well above the 0.8 $M_\odot$ (K km s^{-1} pc^2)$^{-1}$ factor that is generally applied to ULIRGs and SMGs (Downes & Solomon 1998; Solomon & Vanden Bout 2005; Tacconi et al. 2006, 2008) with individual values for ULIRGs typically in the range of 0.3–1.3. The individual values are also somewhat lower than the Milky Way (MW) factor of 4.6 $M_\odot$ (K km s^{-1} pc^2)$^{-1}$, although still consistent within $\sim1\sigma$ for each object.

Combining the three galaxies allows us to exclude the ULIRG-like conversion factor at the 3.7σ level, while the MW-like value is within 1.3σ of our estimate.

This conversion factor in turn allows us to estimate the gas content in the BzK galaxies for which a direct estimate was unfeasible due to larger observational uncertainties. The gas masses and fractions in these three galaxies turn out to be similarly high as in the three galaxies with dynamical estimates (Table 4).

We notice that our α_{CO} traces the total amount of gas, including molecular and atomic hydrogen as well as helium in their respective proportions within the galaxies half-light radii. However, we expect the vast majority of the hydrogen to be molecular given that the high observed densities and expected pressures in the interstellar medium of these galaxies (see, e.g., Blitz & Rosolowsky 2006; Leroy et al. 2008; Obreschkow & Rawlings 2009). This is also consistent with hydrodynamic simulations where more than 90% of the gas mass is molecular, at densities above 100 cm^{-3} and temperatures below $\sim$100 K (F. Bournaud et al. 2010, in preparation).

In summary, our analysis shows the existence of large molecular gas masses in our targets, and a high CO-to-gas mass conversion factor, similar to the one found in the Milky Way. We can estimate the gas mass fractions $f_{gas} = M_{gas}/(M_{gas} + M_{stars})$. For consistency, we apply the average conversion factor of $\alpha_{CO} = 3.6$ to all observed CO luminosities. The gas fractions range from 51% to 66%, with the average being 57% with a dispersion within the sample of 6%. These galaxies clearly have very high gas fractions, with gas accounting for masses that are similar or greater than those of the stars.

The gas fraction appears quite constant within the sample (Figure 18). Given the correlation between L'_{CO} (and thus gas mass) and L_{IR} (or SFR) with a slope above unity, and

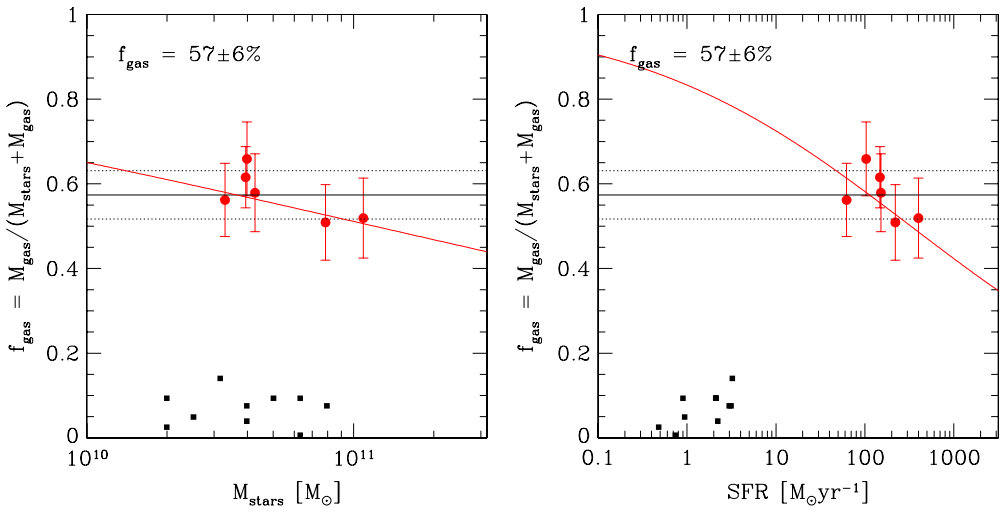

Figure 18. Gas fractions for the six CO-detected BzK galaxies, derived using a MW-like $\alpha_{CO} = 3.6$ are compared to stellar masses (left panel) and SFRs (right panel). The solid and dotted horizontal lines show the average value and the 1σ scatter. The red curves show the expected trend assuming at face value the correlation between L'_{CO} and L_{IR} (hence SFR) and the stellar mass–SFR correlation at $z \gtrsim 1.4$ (see discussion in the text). The black filled squares in the left panel show the molecular gas fraction for local spirals with $M > 2 \times 10^{10}\ M_\odot$ from Leroy et al. (2008), including H_2 and helium (for our BzK galaxies we expect that most of the hydrogen is molecular). From bottom to top, the galaxy IDs are BzK-21000, 12591, 25536, 16000, 17999, and 4171.

(A color version of this figure is available in the online journal.)

the correlation between stellar mass and SFR with a slope slightly below unity, one could expect a gas mass fraction slowly decreasing with increasing stellar mass and SFR. The data are consistent with such a weak trend.

For comparison, the total gas fractions (including H I, H_2, and helium) in local spiral galaxies with the same mass is about 20% (Leroy et al. 2008), and about 7% if including only H_2 and helium (i.e., restricting to the stellar disk). We thus observe a very strong evolution in the gas fractions of disks at fixed stellar mass. Assuming that most of the gas within r_e in BzK galaxies is molecular, this corresponds to an average increase of molecular gas content of a factor of 18, at fixed stellar mass, from $z = 0$ to 1.5. This is very similar to the increase of the SSFR (or the normalization of the stellar mass–SFR relation) between $z = 0$ and 1.5. Hence the increase in SSFR can be consistently explained by the increase of molecular gas content inside star-forming galaxies.

Dividing the gas masses by the SFRs, we estimate gas consumption timescales in the range of 0.3–0.8 Gyr. The SFRs can in principle continue for even longer timescales, once accounting for gas accretion. This confirms that star formation can go on for much longer timescales than expected in rapid, generally merger-driven bursts. The (rotation) dynamical timescale at the half-light radius is $t_{rot} = 2\pi r_e/(v_{FWHM}/2)$, and ranges over 0.1–0.3 Gyr for our galaxies. On average the gas consumption time thus corresponds to 3.5 rotation timescales for the disks at r_e.

6.1. Discussion of Systematic Uncertainties

It is important to investigate possible systematic effects that could be biasing our dynamical mass analysis and the resulting derivation of the α_{CO} conversion factor. Generally speaking, these CO-detected BzK galaxies have bolometric IR luminosities similar to those of local ULIRGs, but we advocate a much larger conversion factor. Several reasons make this quite plausible as these galaxies behave like disk galaxies in many regards—see discussions in Daddi et al. (2008), Dannerbauer et al. (2009), and in the next section. However, we should investigate if there are issues that could have led to an overestimation of the conversion factor.

A first possible issue deals with systematics in the derivation of the dynamical masses. Our analysis is calibrated on clumpy disk numerical modeling, which seems well justified given that our sources are observed to be highly clumpy. If we were to neglect the factor of 1.3 in Equation (2), the combined constraint on α_{CO} would get smaller, but still three times higher than the ULIRG-like value. Nevertheless, this correction factor is unlikely to be a numerical artifact, as it is theoretically justified from the high velocity dispersions observed in high-redshift gas disks (Burkert et al. 2009).

If we interpreted our sources as merging galaxies rather than clumpy disks, the implied dynamical masses would have grown even higher (see, e.g., Tacconi et al. 2008), and so would the conversion factor.

We might also consider systematic effects in the determination of the stellar mass. We have used a bottom-light IMF that is the best choice according to observations in the local universe (Chabrier 2003; see also Kroupa 2002). Several authors have suggested that more top-heavy IMFs might be appropriate in the distant universe (Davé 2008; van Dokkum 2008), which would further decrease the estimated stellar masses and hence increase the conversion factor.

There remains the possibility that these galaxies could contain large reservoirs of old stars, formed at very high redshifts, that could be missed because the light is dominated by young stars. In practice, we would need to postulate hidden stellar mass reservoirs that should increase the total stellar masses by factors of 2–3 in order to bring our estimate of α_{CO} to the ULIRG-like level. However, here we use observations up to the near-IR rest frame (from IRAC) that should correctly retrieve the masses of old stars without such a strong bias. Also, these putative old stellar reservoirs would most likely be in bulges and halos, which actually *cannot* contain most of the stellar mass around $z \sim 2$ disks according to the modeling of Bournaud & Elmegreen (2009). In addition, the existence of the stellar mass–SFR correlations suggests that the appropriate star formation histories for high-redshift galaxies have SFRs that are

rising rapidly with time (e.g., Renzini 2009) so that the galaxies that we observe formed most of their stars quite recently.

Another assumption that we have made is a dark matter fraction of 25% inside the effective radius. There is of course a plausible range around this value. If we change the estimate of the dark matter fraction to 20% (30%) the average α_{CO} would increase (decrease) by about 10%. A survey of local spirals by Pizagno et al. (2005) shows a total-to-stellar mass ratio around two within 2.2 times the exponential disk scale length for galaxies with baryonic masses $\simeq 10^{11}$ $M_{\odot}$, which for an exponential disk corresponds to a total-to-stellar ratio of 1.4 within the half-light radius, i.e., a dark matter fraction of 20%–25%. Padmanabhan et al. (2004) find similar dark matter fractions in massive galaxies and emphasize the fact that higher fraction are found only in low-mass and low-density galaxies. The recent mass models of the Milky Way by Xue et al. (2008) correspond to a dark matter fraction of 23% within the half-light radius, using Navarro–Frenk–White (NFW) profiles for the halo. There is no known reason for a major change with redshift.[13] The observed objects could turn into elliptical galaxies by redshift zero, but the dark matter fraction still remains limited to less than 25%, and likely 15%, within the half-mass radius (e.g., Gnedin & Ostriker 2001). Thus, our choice of 25% lies on the conservative side of the plausible range. A dark matter fraction of 60%, which would lower our α_{CO} to the ULIRG value, appears to be very unlikely.

7. IMPLICATIONS ON STAR FORMATION IN DISK GALAXIES AT HIGH REDSHIFT

7.1. Massive, Extended Reservoirs of Low-excitation Molecular Gas

CO[2–1] detections of two near-IR-selected (BzK) galaxies at $z = 1.5$ were presented in Daddi et al. (2008). We have now observed a total of six galaxies in CO[2–1] and detected all of them. This clearly supports the ubiquity of massive molecular gas reservoirs in these galaxies, a result confirmed by Tacconi et al. (2010).

In our observations, we were able to spatially resolve robustly the CO[2–1] emission in this kind of galaxies and derive typical CO emission FWHM in the range of 6–11 kpc. This is a factor of 2–3 larger than what is found in SMGs (Tacconi et al. 2006, 2008; Bouché et al. 2007). The presence of extended gas disks is quite consistent with our previous finding based on the low CO excitation in these objects (Dannerbauer et al. 2009). These findings are indicative of colder and/or lower density gas than what is found in SMGs, a situation more similar to what is found in local spiral galaxies.

7.2. Normal Star-forming Galaxies at High Redshift as Extended, Clumpy Rotating Disks

Our sample is based on the BzK-selection technique and we have shown it to be representative of "normal," typical star-forming galaxies at high redshift. We now summarize the many pieces of evidence that these CO-detected BzK galaxies are large disk galaxies rather than ongoing violent mergers.

First, we clearly detect double-peaked profiles and the velocity width in the blue- and redshifted components is very similar. This would be a highly contrived coincidence if this was due to a merger: the components would need to have equal mass and be observed at similar inclinations.

Second, the UV rest-frame morphology disfavors ongoing major mergers: in no case do we see evidence for a double-galaxy encounter. The irregular and clumpy morphology could lead one to speculate that this is due to the presence of multiple minor merging events, but in all likelihood we are looking at clumps in single massive disks (Elmegreen et al. 2007, 2009a; Bournaud et al. 2008; Genzel et al. 2008).

Other evidence for rotating disks include the position of these sources in the velocity–size plane. Bouché et al. (2007) used Hα resolved spectroscopy of optical and near-IR-selected galaxies and identified a dichotomy between SMGs and extended disks in such velocity–size diagrams: SMGs have much higher velocities and smaller sizes. Using CO velocity widths and CO sizes for both BzK galaxies and SMGs, we confirm a dichotomy between the two classes: in the notation of Bouché et al., our CO-detected galaxies have "maximum rotational velocities" $v_d = v_{\rm FWHM}/2.35 \lesssim 200$ km s^{-1} and exponential disk scale lengths $r_d > 3$ kpc, while the SMGs in Bouché et al. have $v_d > 200$ km s^{-1} and $r_d < 3$ kpc. The latter are better understood in terms of merging systems, while the former appear consistent with being non-interacting disk galaxies (or interacting only with low-mass satellites).

Further evidence that we are looking at disk galaxies comes from the CO properties. We have already discussed the large spatial sizes of the CO reservoirs, and the low gas excitation. Furthermore, the SFE in these galaxies is considerably lower than that of both SMGs and local ULIRGs, suggesting a different star formation *mode*. The gas depletion timescales are of order of 0.5 Gyr and imply a high duty cycle (see also Daddi et al. 2005, 2007, 2008)—this is quite different from the timescales expected for a merger-induced event that would result in a $\lesssim$100 Myr starburst (Mihos & Hernquist 1996; Greve et al. 2005; Di Matteo et al. 2008). As can be seen from Figure 13, SMGs typically also have depletion timescales of $<$100 Myr.

7.3. Origin of Massive Disks at High Redshift

The fact that we are presumably looking at non-interacting rotating disks instead of ongoing mergers does not in itself imply that these massive disks were not assembled by past mergers. Remnants of major mergers can have massive rotating gas disks, especially when the gas fraction is high (e.g., Robertson & Bullock 2008). Numerical models predict that, under some physical assumptions, merger remnants can contain extended gas disks (e.g., Hopkins et al. 2009). However, Bournaud & Elmegreen (2009) argued that the overall spatial distribution of the mass in high-redshift disks is inconsistent with the majority of them being merger remnants, suggesting that their mass assembly was dominated by relatively smooth mass infall along gas streams (see also Dekel et al. 2009a). This is because the morphology of these disk galaxies, in particular their supermassive star-forming clumps, cannot be accounted for if the main assembly channel is by mergers. Our CO observations add further support to this picture. Indeed, we find extended CO reservoirs with spatial sizes consistent with what is measured from their stellar light. The end product of galaxy mergers is characterized by highly concentrated molecular gas distributions, even when some molecular gas is found in the outer regions. This holds both for early-stage interactions (pre-merger galaxies like Arp 105; Duc et al. 1997), ongoing mergers (like NGC 520; Yun & Hibbard 2001), and merger remnants (like NGC 7252; Hibbard et al. 1994). This dynamical effect

[13] Adiabatic contraction of halos may actually increase the dark matter mass enclosed by a given radius with time, but the effect should be weak between $z = 1.5$ and $z = 0$.

results from the gravitational torquing of the gas, which is well reproduced by numerical simulations (Barnes & Hernquist 1991; Di Matteo et al. 2008) and is independent of the gas fraction. If major mergers played a role in the formation of $z = 1.5$ BzK galaxies, their large molecular disks must have been replenished by the smooth infall of baryons at a rate higher than the merger-driven mass assembly in order to keep extended gas disks. Cold flow-driven galaxy formation, indeed, does predict a large population of massive, extended star-forming disks at high redshift with high gas fractions (e.g., Dekel et al. 2009a).

7.4. Global Properties of Star Formation at High Redshift

In a simple cartoon, the $z = 1.5$ BzK galaxies appear to be disks like local spiral galaxies, but containing a substantially higher gas content and much larger star-forming clumps. A similar comparison holds for SMGs versus local ULIRGs, with the former being the scaled-up version of the latter but having overall higher gas content (Tacconi et al. 2006). Most of the observed properties of the two classes can be understood within this scheme: there is a population of disk galaxies having low-excitation CO, spatially extended gas reservoirs, low SFE (and hence long gas consumption timescales), low SSFR, and optically thin UV emission. These are the familiar spirals in the local universe, and likely most of the near-IR (or optical) selected disk galaxies in the distant universe. Conversely, there are galaxy populations with opposite properties: high CO excitation, compact gas reservoirs, high SFE, high SSFR and with optically thick UV emission. These are the local ULIRGs and high-redshift SMGs, both classes likely corresponding to major (wet) mergers of massive star-forming galaxies.

7.5. New Constraints for Galaxy Formation Models and the IMF

Based on our results of a remarkably low scatter in observed SFE and gas fractions for the CO-detected BzK galaxies, we suggest that the molecular gas content plays an important role in driving the tight stellar mass–SFR correlation in high-redshift sources. A simple scenario may be that the gas properties are tightly connected to that of the underlying dark matter halo, possibly via the regulation of cold gas accretion rates through cosmic times (e.g., Kereš et al. 2005; see also Bouché et al. 2009). This in turn could regulate the amount of star formation in each halo and its time integral, i.e., the stellar mass, which, as a result, is tightly connected. Ultimately, there might be a stellar mass–SFR correlation because the gas content of galaxies tightly correlates with the masses of hosting dark matter halos over cosmological timescales.

Galaxy formation models based on numerical hydrodynamic codes (e.g., Finlator et al. 2006) and semianalytical renditions (e.g., Kitzbichler & White 2007; see Figures 17 and 18 in Daddi et al. 2007a) had indeed predicted the existence of tight correlations between stellar mass and SFR before they were recovered by observations, with roughly a correct slope (or possibly slightly shallower, see, e.g., Daddi et al. 2007a). This is probably one of the rare cases where models of galaxy formation have preceded observations, showing truly predictive power. Also, such models had qualitatively predicted an increase in the normalization of the correlation toward higher redshifts.

However, existing models fail in reproducing the actual magnitude of the normalization increase to $z \sim 2$ (falling short by factors of 3–5 compared to observational estimates; see, e.g., Daddi et al. 2007a; Davé 2008). The SFRs estimated for distant galaxies are generally too high compared to the prediction of models, a fact that has been long known for SMGs (Baugh et al. 2005). Davé (2008) suggest that this discrepancy between models and observations can be solved by adopting substantial evolution in the stellar IMF. This conclusion was also reached by Baugh et al. (2005) in their modeling of SMGs (i.e., for galaxies with extreme SFRs of typically 1000 $M_\odot$ yr^{-1} that have space densities at least an order of magnitude lower than that of near-IR-selected massive galaxies at $z \sim 2$). However, new theoretical frameworks have recently been proposed in which feeding of star formation through cold flow filaments (Dekel et al. 2009b; see also Kereš et al. 2005) can more easily justify high SFRs in distant galaxies. In addition, we have also found large gas reservoirs, reaching 10^{11} $M_\odot$ in some cases, i.e., the gas accounts for a major fraction of the baryons in these sources. We are thus witnessing a phase in galaxy formation in which massive galaxies were truly gas-dominated systems. These high gas masses can explain the high observed SFRs and one does not need to advocate nonstandard IMFs to reduce the SFR, at least for the normal, near-IR-selected (BzK) galaxies. We note that quantitative predictions of the models by Oppenheimer & Davé (2006, 2008) on the gas fractions in galaxies at $z \sim 2$ (with similar stellar masses to our CO-detected galaxies) result in expected gas mass fractions of order of 15%, i.e., much smaller than what we derived. Therefore, our study suggests that the molecular gas fraction in galaxy simulations should be increased in order to reproduce the observed IR luminosities, without necessarily introducing a top-heavy IMF.

8. SUMMARY

We have presented results from a CO[2–1] survey of normal, BzK-selected star-forming galaxies at $z \simeq 1.5$. The analysis of the integrated spectra and the spatially resolved CO observations was made in combination with high-resolution optical imaging and multiwavelength data. We also used appropriate numerical simulations of clumpy disk galaxies (BEE07) to derive dynamical masses and compare them with the observed CO luminosities. The main findings and implications can be summarized as follows.

1. All observed galaxies were detected with high S/Ns. We detected extended CO reservoirs with typical sizes of ∼6–11 kpc, and presented evidence for rotation from spatially resolved CO observations. This is indicative of the molecular gas being situated in disks that are similar in size and shape to the UV rest-frame morphology.
2. We have provided direct evidence for a high α_{CO} conversion factor (relating CO luminosity to gas mass), based on the dynamical masses of the systems. Our results show that the conversion factor of BzK galaxies is high, similar to that of local spirals. Our derived α_{CO} is a factor of 4–5 larger than what has been derived for local ULIRGs and typically used for high-redshift SMGs.
3. Our observations imply high gas fractions, ≃50%–65% of the baryons in our $z \simeq 1.5$ galaxy sample, and quiescent star formation with relatively low SFE and long gas consumption timescales (∼0.5 Gyr).
4. Our results also point to a strong correlation between the molecular gas content and other physical properties of these sources. Once the stellar mass and SFR of a given galaxy are known, the CO luminosities can be predicted to within 40% rms. This and the overall similar SFEs seen in these galaxies

and local spirals lead us to propose a relation between CO luminosity and bolometric luminosity that could allow one to systematically estimate the CO luminosity of massive disk galaxies, presumably at any redshift $z \lesssim 2$ as the relation can fit local and $z = 1.5$ observations with an overall scatter of only 0.25 dex.

5. Our sample consists of normal star-forming galaxies at high redshift, and we have shown that it is representative of the majority of $z > 1$ near-IR-selected star-forming galaxies. Our results shed more light on the nature of these high-redshift disk galaxies. In particular, the large spatial size of the molecular gas reservoirs suggests that they did not assemble mostly through past episodes of violent mergers. Instead, our observations are more consistent with smooth mass infall along cosmic flows and subsequent internal evolution as the main drivers of disk galaxy formation and star formation at high redshift.

This study is based on observations with the IRAM Plateau de Bure Interferometer. IRAM is supported by INSU/CNRS (France), MPG (Germany), and IGN (Spain). We acknowledge the use of GILDAS software (http://www.iram.fr/IRAMFR/GILDAS). We are grateful to Len Cowie for help in cross-checking the spectroscopic redshift of BzK-12591 from Keck observations, prior to our CO follow-up. We thank Claudia Maraston for providing Chabrier IMF models from her library of synthetic stellar populations templates. We thank Padeli Papadopoulos for comments and the anonymous referee for a constructive report. This research was supported by the ERC-StG grant UPGAL 240039. We acknowledge the funding support of French ANR under contracts ANR-07-BLAN-0228, ANR-08-JCJC-0008, and ANR-08-BLAN-0274. Support for this work was provided by NASA, contract number 1224666 issued by JPL, Caltech, under NASA contract 1407. D.R. acknowledges support from NASA through Hubble Fellowship grant HST-HF-51235.01 awarded by the Space Telescope Science Institute, which is operated by the Association of Universities for Research in Astronomy, Inc., for NASA, under contract NAS 5-26555. The work of D.S. was carried out at the Jet Propulsion Laboratory, California Institute of Technology, under a contract with NASA. The simulations were performed using HPC resources from GENCI-CCRT (grant 2009-042192).

REFERENCES

Adelberger, K. L., Steidel, C. C., Shapley, A. E., Hunt, M. P., Erb, D. K., Reddy, N. A., & Pettini, M. 2004, ApJ, 607, 226
Agertz, O., Teyssier, R., & Moore, B. 2009, MNRAS, 397, L64
Alexander, D. M., et al. 2003, AJ, 126, 539
Avni, Y. 1976, ApJ, 210, 642
Barnes, J. E., & Hernquist, L. E. 1991, ApJ, 370, L65
Baugh, C. M., Lacey, C. G., Frenk, C. S., Granato, G. L., Silva, L., Bressan, A., Benson, A. J., & Cole, S. 2005, MNRAS, 356, 1191
Bell, E. F., et al. 2005, ApJ, 625, 23
Binney, J., & Tremaine, S. 2008, Galactic Dynamics (2nd ed.; Princeton, NJ: Princeton Univ. Press)
Blitz, L., & Rosolowsky, E. 2006, ApJ, 650, 933
Bosma, A. 1981, AJ, 86, 1825
Bouché, N., Dekel, A., & Genzel, R. 2009, ApJ, submitted (arXiv:0912.1858)
Bouché, N., et al. 2007, ApJ, 671, 303
Bournaud, F., & Elmegreen, B. G. 2009, ApJ, 694, L158
Bournaud, F., Elmegreen, B. G., & Elmegreen, D. M. 2007, ApJ, 670, 237 (BEE07)
Bournaud, F., et al. 2008, A&A, 486, 741
Burkert, A., et al. 2009, ApJ, submitted (arXiv:0907.4777)
Calzetti, D., Armus, L., Bohlin, R. C., Kinney, A. L., Koornneef, J., & Storchi-Bergmann, T. 2000, ApJ, 533, 682
Caputi, K. I., et al. 2008, ApJ, 680, 939
Carilli, C. L., et al. 2010, ApJ, in press
Casey, C. M., et al. 2009, MNRAS, 399, 121
Ceverino, D., Dekel, A., & Bournaud, F. 2010, MNRAS, in press (arXiv: 0907.3271)
Chabrier, G. 2003, ApJ, 586, L133
Chapman, S. C., Windhorst, R., Odewahn, S., Yan, H., & Conselice, C. 2003, ApJ, 599, 92
Chary, R., & Elbaz, D. 2001, ApJ, 556, 562
Cowie, L. L., Songaila, A., Hu, E. M., & Cohen, J. G. 1996, AJ, 112, 839
Cowie, L. L., et al. 2004, AJ, 127, 3137
Daddi, E., Cimatti, A., Renzini, A., Fontana, A., Mignoli, M., Pozzetti, L., Tozzi, P., & Zamorani, G. 2004a, ApJ, 617, 746
Daddi, E., Dannerbauer, H., Elbaz, D., Dickinson, M., Morrison, G., Stern, D., & Ravindranath, S. 2008, ApJ, 673, L21
Daddi, E., et al. 2004b, ApJ, 600, L127
Daddi, E., et al. 2005, ApJ, 631, L13
Daddi, E., et al. 2007a, ApJ, 670, 156
Daddi, E., et al. 2007b, ApJ, 670, 173
Daddi, E., Dannerbauer, H., Krips, M., Walter, F., Dickinson, M., Elbaz, D., & Morrison, G. E. 2009a, ApJ, 695, L176
Daddi, E., et al. 2009b, ApJ, 694, 1517
Dannerbauer, H., Daddi, E., Riechers, D. A., Walter, F., Carilli, C. L., Dickinson, M., Elbaz, D., & Morrison, G. E. 2009, ApJ, 698, L178
Davé, R. 2008, MNRAS, 385, 147
de Blok, W. J. G., Walter, F., Brinks, E., Trachternach, C., Oh, S.-H., & Kennicutt, R. C. 2008, AJ, 136, 2648
Dekel, A., Sari, R., & Ceverino, D. 2009a, ApJ, 703, 785
Dekel, A., et al. 2009b, Nature, 457, 451
Di Matteo, P., Bournaud, F., Martig, M., Combes, F., Melchior, A.-L., & Semelin, B. 2008, A&A, 492, 31
Downes, D., & Solomon, P. M. 1998, ApJ, 507, 615
Duc, P.-A., Brinks, E., Wink, J. E., & Mirabel, I. F. 1997, A&A, 326, 537
Elbaz, D., et al. 2007, A&A, 468, 33
Elmegreen, B. G., & Burkert, A. 2010, ApJ, 712, 294
Elmegreen, B. G., & Elmegreen, D. M. 2005, ApJ, 627, 632
Elmegreen, B. G., Elmegreen, D. M., Fernandez, M. X., & Lemonias, J. J. 2009a, ApJ, 692, 12
Elmegreen, D. M., Elmegreen, B. G., Marcus, M. T., Shahinyan, K., Yau, A., & Petersen, M. 2009b, ApJ, 701, 306
Elmegreen, D. M., Elmegreen, B. G., Ravindranath, S., & Coe, D. A. 2007, ApJ, 658, 763
Erb, D. K., Shapley, A. E., Pettini, M., Steidel, C. C., Reddy, N. A., & Adelberger, K. L. 2006, ApJ, 644, 813
Finlator, K., Davé, R., Papovich, C., & Hernquist, L. 2006, ApJ, 639, 672
Flores, H., Hammer, F., Puech, M., Amram, P., & Balkowski, C. 2006, A&A, 455, 107
Förster-Schreiber, N. M., et al. 2009, ApJ, in press (arXiv:0903.1872)
Frayer, D. T., et al. 2008, ApJ, 680, L21
Frayer, D. T., et al. 2009, AJ, 138, 1261
Genzel, R., et al. 2008, ApJ, 687, 59
Giavalisco, M., et al. 2004, ApJ, 600, L93
Gonzalez, A. H., Clowe, D., Bradač, M., Zaritsky, D., Jones, C., & Markevitch, M. 2009, ApJ, 691, 525
Gnedin, O. Y., & Ostriker, J. P. 2001, ApJ, 561, 61
Greggio, L., Renzini, A., & Daddi, E. 2008, MNRAS, 388, 829
Greve, T. R., Ivison, R. J., & Papadopoulos, P. P. 2003, ApJ, 599, 839
Greve, T. R., et al. 2005, MNRAS, 359, 1165
Hatsukade, B., et al. 2009, PASJ, 61, 487
Hayashi, M., et al. 2009, ApJ, 691, 140
Hibbard, J. E., Guhathakurta, P., van Gorkom, J. H., & Schweizer, F. 1994, AJ, 107, 67
Hopkins, A. M., & Beacom, J. F. 2006, ApJ, 651, 142
Hopkins, A. M., & Beacom, J. F. 2008, ApJ, 682, 1486
Hopkins, P. F., et al. 2009, MNRAS, 397, 802
Immeli, A., Samland, M., Gerhard, O., & Westera, P. 2004, A&A, 413, 547
Kennicutt, R. C., Jr. 1998, ARA&A, 36, 189
Kereš, D., Katz, N., Weinberg, D. H., & Davé, R. 2005, MNRAS, 363, 2
Kitzbichler, M. G., & White, S. D. M. 2007, MNRAS, 376, 2
Kovács, A., Chapman, S. C., Dowell, C. D., Blain, A. W., Ivison, R. J., Smail, I., & Phillips, T. G. 2006, ApJ, 650, 592
Kroupa, P. 2002, Science, 295, 82
Le Borgne, D., Elbaz, D., Ocvirk, P., & Pichon, C. 2009, A&A, 504, 727
Leroy, A. K., Walter, F., Brinks, E., Bigiel, F., de Blok, W. J. G., Madore, B., & Thornley, M. D. 2008, AJ, 136, 2782
Leroy, A. K., et al. 2009, AJ, 137, 4670
Magdis, G. E., Rigopoulou, D., Huang, J., & Fazzio, G. 2010, MNRAS, 401, 1521

Magnelli, B., Elbaz, D., Chary, R. R., Dickinson, M., Le Borgne, D., Frayer, D. T., & Willmer, C. N. A. 2009, A&A, 496, 57
Maraston, C. 2005, MNRAS, 362, 799
Maraston, C., Daddi, E., Renzini, A., Cimatti, A., Dickinson, M., Papovich, C., Pasquali, A., & Pirzkal, N. 2006, ApJ, 652, 85
Mihos, J. C., & Hernquist, L. 1996, ApJ, 464, 641
Morrison, G. E., et al. 2010, ApJS, submitted
Noeske, K. G., et al. 2007, ApJ, 660, L43
Obreschkow, D., & Rawlings, S. 2009, ApJ, 696, L129
Onodera, M., et al. 2010, ApJ, submitted
Oppenheimer, B. D., & Davé, R. 2006, MNRAS, 373, 1265
Oppenheimer, B. D., & Davé, R. 2008, MNRAS, 387, 577
Padmanabhan, N., et al. 2004, New Astron., 9, 329
Pannella, M., et al. 2009, ApJ, 698, L116
Papadopoulos, P. P., Isaak, K. G., & van der Werf, P. P. 2007, ApJ, 668, 815
Peng, C. Y., Ho, L. C., Impey, C. D., & Rix, H.-W. 2002, AJ, 124, 266
Pizagno, J., et al. 2005, ApJ, 633, 844
Pope, A., et al. 2006, MNRAS, 370, 1185
Pope, A., et al. 2008, ApJ, 675, 1171
Renzini, A. 2009, MNRAS, 398, L58
Riechers, D. A., et al. 2006, ApJ, 650, 604
Robertson, B. E., & Bullock, J. S. 2008, ApJ, 685, L27
Solomon, P. M., Downes, D., Radford, S. J. E., & Barrett, J. W. 1997, ApJ, 478, 144
Solomon, P. M., & Vanden Bout, P. A. 2005, ARA&A, 43, 677
Stark, D. P., Ellis, R. S., Bunker, A., Bundy, K., Targett, T., Benson, A., & Lacy, M. 2009, ApJ, 697, 1493
Steidel, C. C., Shapley, A. E., Pettini, M., Adelberger, K. L., Erb, D. K., Reddy, N. A., & Hunt, M. P. 2004, ApJ, 604, 534
Tacconi, L. J., et al. 2006, ApJ, 640, 228
Tacconi, L. J., et al. 2008, ApJ, 680, 246
Tacconi, L. J., et al. 2010, Nature, 463, 781
Trachternach, C., de Blok, W. J. G., Walter, F., Brinks, E., & Kennicutt, R. C. 2008, AJ, 136, 2720
van Dokkum, P. G. 2008, ApJ, 674, 29
van Dokkum, P. G., et al. 2006, ApJ, 638, L59
Walter, F., Brinks, E., de Blok, W. J. G., Bigiel, F., Kennicutt, R. C., Thornley, M. D., & Leroy, A. 2008, AJ, 136, 2563
Weiß, A., Downes, D., Walter, F., & Henkel, C. 2005, A&A, 440, L45
Weiß, A., Downes, D., Walter, F., & Henkel, C. 2007, in ASP Conf. Ser. 375, From Z-Machines to ALMA: (Sub)Millimeter Spectroscopy of Galaxies, ed. A. J. Baker et al. (San Francisco, CA: ASP), 25
Wilson, C. D., et al. 2009, ApJ, 693, 1736
Wolfe, A. M., Turnshek, D. A., Smith, H. E., & Cohen, R. D. 1986, ApJS, 61, 249
Xue, X. X., et al. 2008, ApJ, 684, 1143
Yao, L., Seaquist, E. R., Kuno, N., & Dunne, L. 2003, ApJ, 588, 771
Yun, M. S., & Hibbard, J. E. 2001, ApJ, 550, 104